CrossMark

A Particle Module for the PLUTO Code. I. An Implementation of the MHD–PIC Equations

A. Mignone[1], G. Bodo[2] ⬦, B. Vaidya[3] ⬦, and G. Mattia[1]
[1] Physics Department, University of Turin, via Pietro Giuria 1 (I-10125) Torino, Italy
[2] INAF, Osservatorio Astrofisico di Torino, Strada Osservatorio 20, Pino Torinese I-10025, Italy
[3] Centre of Astronomy, Indian Institute of Technology Indore, Khandwa Road, Simrol, Indore 453552, India

Abstract

We describe an implementation of a particle physics module available for the PLUTO code appropriate for the dynamical evolution of a plasma consisting of a thermal fluid and a nonthermal component represented by relativistic charged particles or cosmic rays (CRs). While the fluid is approached using standard numerical schemes for magnetohydrodynamics, CR particles are treated kinetically using conventional Particle-In-Cell (PIC) techniques. The module can be used either to describe test-particle motion in the fluid electromagnetic field or to solve the fully coupled magnetohydrodynamics (MHD)–PIC system of equations with particle backreaction on the fluid as originally introduced by Bai et al. Particle backreaction on the fluid is included in the form of momentum–energy feedback and by introducing the CR-induced Hall term in Ohm's law. The hybrid MHD–PIC module can be employed to study CR kinetic effects on scales larger than the (ion) skin depth provided that the Larmor gyration scale is properly resolved. When applicable, this formulation avoids resolving microscopic scales, offering substantial computational savings with respect to PIC simulations. We present a fully conservative formulation that is second-order accurate in time and space, and extends to either the Runge–Kutta (RK) or the corner transport upwind time-stepping schemes (for the fluid), while a standard Boris integrator is employed for the particles. For highly energetic relativistic CRs and in order to overcome the time-step restriction, a novel subcycling strategy that retains second-order accuracy in time is presented. Numerical benchmarks and applications including Bell instability, diffusive shock acceleration, and test-particle acceleration in reconnecting layers are discussed.

Key words: acceleration of particles – instabilities – magnetohydrodynamics (MHD) – methods: numerical – plasmas – shock waves

1. Introduction

High-energy astrophysical phenomena are connected to environments where matter exists under extreme conditions, leading to powerful releases of electromagnetic radiation from the radio to the optical, X-ray, and γ-ray wavebands. Typical examples are found in blazar jets (Böttcher 2007; Giannios 2013), gamma-ray bursts (GRBs; see, e.g., Giannios 2008; McKinney & Uzdensky 2012; Beniamini & Piran 2014; Beniamini & Giannios 2017), pulsar wind nebulae (PWNe; see, e.g., Bucciantini et al. 2011; Kargaltsev et al. 2015; Olmi et al. 2016, and references therein), and supernova remnants (SNRs; see e.g., Amato & Blasi 2009; Morlino et al. 2013; Caprioli & Spitkovsky 2014b, and references therein), among others. The observed radiation presents typical signatures of nonthermal emission processes, such as synchrotron and inverse Compton, typically arising from charged particles accelerated by electromagnetic fields.

A comprehensive modeling of such systems is a challenging task because physical mechanisms operate over an enormous range of spatial and temporal scales stretching from the microphysical—where energy dissipation occurs and emission originates—to the macroscopic—where dynamics trigger dissipation. Owing to the complexity of the interactions, state-of-the-art modeling and key achievements in this field have been obtained mostly through time-dependent numerical computations. For these reasons, our current understanding of astrophysical systems is limited by the range of scales beyond which one or more model assumptions breaks down or when computational resources become prohibitive.

On the one hand, fluid models such as magnetohydrodynamics (MHD) have been extensively used to investigate the large-scale dynamics of high-energy astrophysical environments in jets (e.g., Rossi et al. 2008; Mignone et al. 2010a, 2013; Mizuno et al. 2012; Porth 2013; English et al. 2016; Barniol Duran et al. 2017), PWNe (e.g., Del Zanna et al. 2006), and also SNRs (Orlando et al. 2009; Miceli et al. 2016). Because of its nature, however, the fluid approach is applicable on scales much larger than the Larmor radius, and it cannot capture important kinetic effects relevant to the microscale. On the other hand, Particle-in-Cell (PIC; see the book by Birdsall & Langdon 2004) codes provide the most self-consistent approach to modeling plasma dynamics at small scales (e.g., Chang et al. 2008; Sironi et al. 2013; Sironi & Spitkovsky 2014). However, PIC codes must resolve the electron skin depth, which, in most cases, is several orders of magnitude smaller than the overall size of a typical astrophysical system. Even with the most powerful supercomputers, PIC simulations become prohibitively expensive for describing astrophysical systems at larger scales. Alternatively, hybrid codes that treat ions as particles and electrons as fluid (Gargaté et al. 2007; Kunz et al. 2014) are commonly used in space physics and laboratory plasma. Hybrid methods cannot capture kinetic effects at the electron scale, and the temporal and spatial scales are limited in resolution by the ion inertial length.

Recently, Bai et al. (2015) have proposed yet another approach, called the MHD–PIC method, to describe the interaction between a collisionless thermal plasma and a population of nonthermal cosmic-ray particles (CRs; typically

ions). The same approach has also been recently employed in the work by van Marle et al. (2018) to study magnetic field amplification and particle acceleration near nonrelativistic astrophysical shocks. In that study, the authors generalize the MHD–PIC approach to any type of suprathermal particle (electrons and ions). The MHD–PIC model, which can be formally derived by considering a three-component plasma in which thermal electrons are massless, does not capture the electron physics, and it can be used to describe the kinetic effects of nonthermal ions on scales that are tied only to the gyration radius and not to the inertial skin depth.

In the present work, we describe the numerical implementation of the MHD–PIC particle module in the PLUTO code for astrophysical fluid dynamics (Mignone et al. 2007, 2012) while providing, at the same time, some new implementation strategies that allow our hybrid framework to be employed with more general second-order time-stepping schemes and to improve in terms of accuracy. In addition, the presented module can also be used to model the dynamics of charged test particles in a time-dependent magnetized fluid with straightforward generalization to the relativistic case. Our numerical framework is part of a more general fluid–particle module, and a companion work (Vaidya et al. 2018, hereafter Paper II) presents a different hybrid scheme for the modeling of nonthermal spectral signatures from highly energetic electrons embedded in a thermal MHD plasma using Lagrangian particles with a time-dependent energy distribution. A brief description, together with applications to astrophysical jets, has been presented in Vaidya et al. (2016).

This paper is organized as follows. The MHD–PIC equations describing the evolution of the composite fluid+CR system are discussed in Section 2, while the numerical implementation is described in Section 3. Numerical benchmarks and applications, for both the full MHD–PIC composite system (including feedback) and the test-particle implementation (without feedback), are presented in Section 4. A summary is given in Section 5.

2. The MHD–PIC Equations

The MHD–PIC approach was recently developed by Bai et al. (2015) to describe the dynamical interaction between a thermal plasma and a nonthermal population of collisionless CRs. While the thermal component, which comprises ions and massless electrons, is described through a fluid approach using shock-capturing MHD methods, CR particles (representing energetic ions or electrons) are treated kinetically using conventional PIC techniques. This formalism aims to capture the kinetic effects of CR particles without the need to resolve the plasma skin depth, as is typically required by PIC codes. In the MHD–PIC formalism, only the Larmor (gyration) scale must be properly resolved instead. This extends the range of applicability to much larger spatial (and temporal) scales when compared to the standard PIC approach, inasmuch as the particle gyroradius largely exceeds the plasma skin depth, $c/\omega_{pi} \approx 2.27 \times 10^7/\sqrt{n_i}$ cm.

The thermal plasma is described by the single-fluid model, which is obtained by averaging the two fluid equations for ions and massless electrons. The derivation, which can also be found in many plasma physics textbooks, is given in Appendix A because of its length. The relevant Equations, (91)–(93), include the effect of CRs via the condition of charge neutrality for the composite system (fluid+CR) and the

definition of the total current density,

$$q_g + q_{CR} = q_e + q_i + q_{CR} = 0, \tag{1}$$

$$\boldsymbol{J}_g + \boldsymbol{J}_{CR} = \boldsymbol{J} = \frac{c}{4\pi}\nabla \times \boldsymbol{B}, \tag{2}$$

where $q_g = q_i + q_e$ is the charge density of the thermal plasma (Equation (95)), q_{CR} is the CR charge density, while $\boldsymbol{J}_{CR} \equiv q_{CR}\boldsymbol{v}_{CR}$ is the CR current density.

Ignoring contributions from the heat flux vector and the viscous stress tensor and taking advantage of Equations (1) and (2) and a straightforward manipulation of Equations (91)–(93), which are properly augmented by Faraday's law of induction, lead to the quasi-conservative form of the MHD–PIC equations:

$$\frac{\partial \rho}{\partial t} + \nabla \cdot (\rho \boldsymbol{v}_g) = 0, \tag{3}$$

$$\frac{\partial (\rho \boldsymbol{v}_g)}{\partial t} + \nabla \cdot \mathsf{T}_m = -\boldsymbol{F}_{CR}, \tag{4}$$

$$\frac{\partial \boldsymbol{B}}{\partial t} + \nabla \times c\boldsymbol{E} = 0, \tag{5}$$

$$\frac{\partial E_g}{\partial t} + \nabla \cdot (\rho H \boldsymbol{v}_g + \boldsymbol{S}) = -\boldsymbol{v}_g \cdot \boldsymbol{F}_{CR}. \tag{6}$$

Here, ρ and $\boldsymbol{v}_g$ represent, respectively, the single-fluid density and velocity (Equations (94) and (89)), which, in the limit of massless electrons, can be trivially identified with those of the ions, i.e., $\rho \to \rho^{(i)}$ and $\boldsymbol{v}_g \to \boldsymbol{v}^{(i)}$. The total energy density E_g is expressed as the sum of kinetic, thermal, and magnetic contributions,

$$E_g = \frac{1}{2}\rho \boldsymbol{v}_g^2 + \frac{3}{2}p + \frac{\boldsymbol{B}^2}{8\pi}, \tag{7}$$

while ρH is the gas enthalpy,

$$\rho H = \left(\frac{1}{2}\rho \boldsymbol{v}_g^2 + \frac{5}{2}p\right)\boldsymbol{v}_g. \tag{8}$$

The gas pressure p, as shown in Appendix A, can be expressed as the sum of the ion and pressure terms of the original two-fluid equations. Finally, T_m defines the momentum flux tensor,

$$\mathsf{T}_m = \rho \boldsymbol{v}_g \boldsymbol{v}_g - \frac{\boldsymbol{B}\boldsymbol{B}}{4\pi} + \mathsf{I}\left(p + \frac{\boldsymbol{B}^2}{8\pi}\right), \tag{9}$$

where I is the unit tensor, $\boldsymbol{B}$ is the magnetic field, $\boldsymbol{S} = c\boldsymbol{E} \times \boldsymbol{B}/4\pi$ is the Poynting vector, and $\boldsymbol{E}$ is the electric field.

The force experienced by the fluid from the CR appears on the right-hand side of Equation (4), and it is the opposite of the Lorentz force experienced by the particles,

$$\boldsymbol{F}_{CR} = q_{CR}\boldsymbol{E} + \frac{1}{c}\boldsymbol{J}_{CR} \times \boldsymbol{B}. \tag{10}$$

Thus, the last term on the right-hand side of Equation (6) is interpreted as the opposite of the energy gained by the CRs due to the work done by the Lorentz force (see Equation (17) in Bai et al. 2015).

The electric field $\boldsymbol{E}$ can be directly obtained from Ohm's law, which is expressed through the electron equation of motion, Equation (85), in the limit $\rho^{(e)} \to 0$. Using the

definition of the total current, Equation (2); the second equation in Equation (95); and the definition of J_{CR}, together with the fact that $v^{(i)} \to v_g$, yields

$$
cE = -v_g \times B - \frac{1}{q_e} J \times B
$$
$$
- \frac{q_{CR}}{|q_e|}(v_{CR} - v_g) \times B + \frac{c}{q_e} \nabla \cdot \mathcal{P}^{(e)}. \quad (11)
$$

In Equation (11), the first term on the right-hand side is the standard convective term, the second is the Hall term, the third describes the relative drift between the CRs and fluid, which will be referred to as the CR-Hall term, and the last term is the electron-pressure term. As noted by Bai et al. (2015), at scales much larger than the ion skin depth, both the standard Hall term and the electron-pressure terms can be safely ignored, and the final form of Ohm's law is then

$$
cE = -v_g \times B - R(v_{CR} - v_g) \times B, \quad (12)
$$

where

$$
R = \frac{q_{CR}}{|q_e|} = \frac{q_{CR}}{q_i + q_{CR}} \quad (13)
$$

is the charge density ratio between CRs and electrons, and the regime in which the described formalism is valid demands $R \ll 1$. The second equality can be recovered with the aid of the charge neutrality condition, Equation (1).

Using the expression for the electric field, Equation (12), the CR force (Equation (10)) can be rewritten as

$$
F_{CR} = (1 - R)\left(q_{CR}E_0 + \frac{1}{c}J_{CR} \times B\right), \quad (14)
$$

where $E_0 = -v_g \times B/c$ is the convective electric field. Expression (14) is more convenient for computational purposes. Likewise, combining Equations (10) and (14) yields the following expression for the total electric field,

$$
E = E_0 - \frac{F_{CR}}{q_i}. \quad (15)
$$

The charge density of the thermal ions q_i is expressed in terms of the charge to mass ratio for the ions,

$$
\alpha_i \equiv \left(\frac{e}{mc}\right)_i, \quad (16)
$$

so that $q_i/c = \alpha_i \rho$, where ρ is the gas density. A similar expression holds for the CR charge density; see Section 2.1.

2.1. Particle Equations of Motion

According to the PIC formalism (for a review, see, e.g., Lapenta 2012), computational particles (CRs) represent clouds of physical particles that are close to each other in phase space. CR particles are defined in terms of their spatial coordinates x_p and velocity v_p, which are governed by the equation of motion

$$
\begin{cases} \frac{dx_p}{dt} = v_p \\ \frac{d(\gamma v)_p}{dt} = \alpha_p(cE + v_p \times B) \end{cases}, \quad (17)
$$

where $\gamma = 1/\sqrt{1 - v_p^2/\mathbb{C}^2}$ is the Lorentz factor whereas

$$
\alpha_p \equiv \left(\frac{e}{mc}\right)_p \quad (18)
$$

is the CR charge to mass ratio. Here and in the following, the suffix p will be used to label a single particle. Using Equation (18), the charge density of an individual particle q_p can be written as $q_p/c = \alpha_p \varrho_p$, where ϱ_p is the actual mass density contribution of a single CR particle.

Since the actual speed of light does not explicitly appear in the MHD equations, we use $\mathbb{C}$ to specify an artificial value for the speed of light, which, for consistency, must be greater than any characteristic signal velocity. The electric and magnetic fields E and B are computed from the magnetized fluid and must be properly interpolated at the particle position. This is described in Section 3.3.

3. Numerical Implementation

We now provide a detailed description of the numerical method employed to solve the MHD–PIC equations, Equations (3)–(6), in the PLUTO code. The solution methods feature an MHD solver already present in the code (modified by the presence of additional terms describing the particle backreaction onto the gas) coupled to a particle integrator.

Fluid quantities such as density, magnetic field, and so forth are discretized on a computational grid with cell indices $i \equiv (i, j, k)$ and stored as three-dimensional arrays. By contrast, particles (being meshless quantities) are held in memory using a doubly linked list consisting of sequentially linked node structures. Each node contains the particle itself and pointers to the previous and to the next node in the sequence. In a linked list, elements can be inserted or removed in a straightforward way, and shuffling operations can be easily performed by changing pointers. Besides, different types of particle data structures can be employed. These features make the linked list approach very flexible, and we have adopted this as a general implementation strategy shared by all particle modules in the PLUTO code, including the Lagrangian particle module described in Paper II.

3.1. MHD Integrators

The numerical solution of the MHD–PIC equations has been implemented by modifying two of the available second-order time-stepping algorithms available in the code. The first one features the corner transport upwind (CTU) scheme (Colella 1990; Gardiner & Stone 2005; Mignone et al. 2012) and also presents an extension of the scheme to the standard second-order total variation diminishing Runge–Kutta (RK2).

Both implementations are second-order accurate in time and space, and conserve momentum and energy to machine accuracy for the composite gas+particle system.

The magnetic field is evolved using constrained transport (CT), although our formulation can be extended to other divergence-cleaning methods (such as those presented in Mignone & Tzeferacos 2010; Mignone et al. 2010b) in a straightforward manner.

3.1.1. CTU Time Stepping

We now provide a schematic description of the the CTU method; we refer the reader to Appendix B for a more detailed

description. The scheme consists of a first predictor step where time-centered states are constructed according to

$$U_i^{n+\frac{1}{2}} = U_i^n + \frac{\Delta t^n}{2}\mathcal{L}_i(U^*, \boldsymbol{F}_{CR}^n) + \frac{\Delta t^n}{2}S_{CR,i}^n, \qquad (19)$$

where $U = (\rho, \rho\boldsymbol{v}_g, \boldsymbol{B}, E_g)$ denotes the array of conserved quantities, U^* is the normal predictor state, $\mathcal{L}$ is a conservative flux-difference operator,

$$\mathcal{L}_i(U^*, \boldsymbol{F}_{CR}^n) = -\sum_d \frac{1}{\Delta x_d}(\mathcal{F}_{i+\frac{1}{2}\hat{e}_d} - \mathcal{F}_{i+\frac{1}{2}\hat{e}_d}), \qquad (20)$$

with $d = x, y, z$ labeling the direction, while

$$S_{CR,i}^n = (0, -\boldsymbol{F}_{CR}, 0, -\boldsymbol{F}_{CR} \cdot \boldsymbol{v}_g)_i^n \qquad (21)$$

accounts for the source terms in the momentum and energy equations, Equations (4) and (6), respectively. The fluxes $\mathcal{F}_{i\pm\frac{1}{2}\hat{e}_d}$ in Equation (20) are computed by solving a Riemann problem at cell interfaces and by adding the CR contribution terms in the induction and energy equations.

The CR force term is computed using Equation (14) by depositing individual particle charges and currents on the grid,

$$\left(\frac{q_{CR}}{c}\right)_i = \sum_p W(\boldsymbol{x}_i - \boldsymbol{x}_p)\alpha_p\varrho_p$$
$$\left(\frac{\boldsymbol{J}_{CR}}{c}\right)_i = \sum_p W(\boldsymbol{x}_i - \boldsymbol{x}_p)\alpha_p\varrho_p\boldsymbol{v}_p, \qquad (22)$$

where α_p is defined in Equation (18) whereas $W()$ are weight functions (see Section 3.3).

Particles are then evolved for a full step (see Section 3.2) using the electromagnetic fields at the midpoint time level:

$$\begin{pmatrix}\boldsymbol{x}_p\\\boldsymbol{u}_p\end{pmatrix}^{n+1} = \begin{pmatrix}\boldsymbol{x}_p\\\boldsymbol{u}_p\end{pmatrix}^n + \Delta t^n\begin{pmatrix}\boldsymbol{v}_p\\\boldsymbol{a}_p\end{pmatrix}^{n+\frac{1}{2}}, \qquad (23)$$

where $\boldsymbol{x}_p$ and $\boldsymbol{u}_p = \gamma_p\boldsymbol{v}_p$ are, respectively, the spatial coordinate and four-velocity of the pth particle. Here, $\boldsymbol{a}_p \equiv \boldsymbol{a}_p (\boldsymbol{x}_p, \boldsymbol{u}_p, U, \boldsymbol{F}_{CR})$ is a compact expression for the Lorentz acceleration, given by the second equation in Equation (17), showing its dependence on both particle and fluid quantities. After CRs have been evolved for a full time step, the total momentum and energy change of a single particle can be computed as

$$\Delta\boldsymbol{m}_p = \varrho_p(\boldsymbol{u}_p^{n+1} - \boldsymbol{u}_p^n)$$
$$\Delta E_{k,p} = \varrho_p(E_{k,p}^{n+1} - E_{k,p}^n), \qquad (24)$$

where $E_{k,p} = (\gamma_p - 1)\mathbb{C}^2$ is the (specific) kinetic energy of a single particle. We then deposit the opposite of these quantities on the grid, allowing momentum and energy feedback to be computed from the particle locations at the half-step:

$$S_{CR,i}^{n+\frac{1}{2}} = -\sum_p \frac{W(\boldsymbol{x}_i - \boldsymbol{x}_p^{n+\frac{1}{2}})}{\Delta t^n}\begin{pmatrix}0\\\Delta\boldsymbol{m}_p\\0\\\Delta E_{k,p}\end{pmatrix}. \qquad (25)$$

As pointed out by Bai et al. (2015), this ensures the exact conservation of the total momentum and energy of the composite gas+CR system.

In the corrector step, fluid quantities are finally evolved for a full step,

$$U_i^{n+1} = U_i^n + \Delta t^n\mathcal{L}_i(U^{n+\frac{1}{2}}, \boldsymbol{F}_{CR}^{n+\frac{1}{2}})$$
$$+ \Delta t^n S_{CR,i}^{n+\frac{1}{2}}, \qquad (26)$$

where $\boldsymbol{F}_{CR}^{n+\frac{1}{2}}$ is given by the opposite of the momentum component of the source term, Equation (25). This completes our derivation of the CTU scheme (more details can be found in Appendix B).

3.1.2. Runge–Kutta Time Stepping

Runge–Kutta (RK) time-stepping methods are based on the method of lines in which the spatial discretization is considered separately from the temporal evolution that is left continuous in time. Equations (3)–(6) are then discretized as regular ordinary differential equations based on predictor–corrector steps.

We consider the second-order RK method (RK2), which consists of a first predictor step in which the fluid is advanced by a full step:

$$U_i^* = U_i^n + \Delta t^n\mathcal{L}_i(U^n, \boldsymbol{F}_{CR}^n) + \Delta t^n S_{CR,i}^n. \qquad (27)$$

Particles are then evolved using Equation (23), where the half-time level fluid variables are computed from the arithmetic average of the conservative variables at level n and the predicted ones,

$$U_i^{n+\frac{1}{2}} = \frac{U_i^n + U_i^*}{2}. \qquad (28)$$

The final corrector step employs a trapezoidal rule for the flux terms and a midpoint rule for the sources:

$$U_i^{n+1} = U_i^n + \Delta t^n\frac{\mathcal{L}_i(U^n, \boldsymbol{F}_{CR}^n) + \mathcal{L}_i(U^*, \boldsymbol{F}_{CR}^*)}{2}$$
$$+ \Delta t^n S_{CR,i}^{n+\frac{1}{2}}. \qquad (29)$$

In the previous equation, $\boldsymbol{F}_{CR}^* = 2\boldsymbol{F}_{CR}^{n+\frac{1}{2}} - \boldsymbol{F}_{CR}^n$ is obtained by simple extrapolation while $\boldsymbol{F}_{CR}^{n+\frac{1}{2}}$ is computed using the opposite of the momentum component in Equation (25). Momentum and energy feedback at the half-time level are accounted for by $S_{CR,i}^{n+\frac{1}{2}}$ and computed as for the CTU scheme using Equation (25).

For implementation purposes, it is more convenient to rewrite Equation (29), using Equation (27), as

$$U_i^{n+1} = \frac{U_i^n + U_i^*}{2} + \Delta t\frac{\mathcal{L}_i(U^*, \boldsymbol{F}_{CR}^*) + S_{CR,i}^*}{2}, \qquad (30)$$

where $S_{CR,i}^* = 2S_{CR,i}^{n+\frac{1}{2}} - S_{CR,i}^n$.

3.2. Particle Mover

Particles' positions and velocities are assumed to be known at the same time level n rather than being staggered in time. This allows the code to employ a variable time step as is typically the case in fluid simulations. Equation (17) is solved by means of a standard Boris pusher, which is essentially an

implicit-position Verlet algorithm, cast as

$$x_p^{n+\frac{1}{2}} = x_p^n + \frac{\Delta t^n}{2} v_p^n \qquad \text{(drift)}$$

$$u_p^- = u_p^n + \frac{h}{2} c E^{n+\frac{1}{2}} \qquad \text{(kick)}$$

$$u_p^+ = u_p^- + 2 \frac{u_p^- + u_p^- \times b}{1 + b^2} \times b \quad \text{(rotate)}$$

$$u^{n+1} = u_p^+ + \frac{h}{2} c E^{n+\frac{1}{2}} \qquad \text{(kick)}$$

$$x_p^{n+1} = x_p^{n+\frac{1}{2}} + \frac{\Delta t^n}{2} v_p^{n+1} \qquad \text{(drift),} \qquad (31)$$

where $u_p = \gamma_p v_p$ is the particle four-velocity, $h = \alpha_p \Delta t^n$, while $b = (h/2) B^{n+\frac{1}{2}}/\gamma^{n+\frac{1}{2}}$. Electromagnetic fields are interpolated at the particle half-step position $x^{n+\frac{1}{2}}$ using Equation (45). Since interpolation at the particle position does not necessarily preserve the orthogonality between E and B (when the electric field is obtained from Equations (12) or (15)), a cleaning step is required to remove non-orthogonal components from the electric field,

$$E \leftarrow E - (E \cdot B) \frac{B}{B^2}. \qquad (32)$$

Note that the rotation does not change the particle energy, and therefore $\gamma^{n+\frac{1}{2}}$ is obtained directly from u_p^-.

The time-step restriction is computed by requiring that no particle travels more than N_{max} zones and that the Larmor scale is resolved with more than one cycle:

$$\Delta t_p^{-1} = \max_p \left[\max_d \left(\frac{|\hat{e}_d \cdot v_p^{n+\frac{1}{2}}|}{N_{max} \Delta x_d} \right), \frac{\Omega_{\perp,p}}{\epsilon_L} \right], \qquad (33)$$

where the first maximum extends to all particles, $v_p^{n+\frac{1}{2}}$ is the half-time level averaged velocity, $\Omega_{\perp,p} = \alpha_p B_\perp/\gamma_p$ is the Larmor frequency, while

$$B_\perp = \sqrt{B^2 - \frac{(v_p \cdot B)^2}{v_p \cdot v_p}} \qquad (34)$$

is the transverse component of the magnetic field. In Equation (33), we choose $N_{max} = 1.8$ and $\epsilon_L = 0.3$ as safety factors.

3.2.1. CR Predictor Step

We note that the particle mover given by Equation (31) requires knowledge of the electric field at the half-time step. In the case of test particles, this is not a problem, since the electric field depends solely on the fluid and can be easily be determined.

However, in the MHD–PIC system, the electric field (see Equation (12)) is comprised of the convective and CR-Hall terms, but only the former is known at the half-time level $t^n + \Delta t^n/2$ while the latter can only be computed at the base time level t^n. Formally, therefore, we expect the integration scheme to be only first-order accurate in time. We point out that for the conditions under which the MHD–PIC formalism is valid ($R \ll 1$), the CR-Hall term is generally unimportant but it

may become comparable to the convective term for large CR streaming velocities.

In order to achieve full second-order accuracy, we propose a predictor step where particles are evolved for half a time increment using a first-order explicit–implicit scheme,

$$u_p^{*,n} = u_p^n + \frac{h}{2} \left(c E^n + \frac{u_p^{*,n}}{\gamma_p^{*,n}} \times B^{*,n} \right) \qquad (35)$$

where the notation $u_p^{*,n}$ stands for the half-time level predicted value while $h = \alpha_p \Delta t$. Since the $v \times B$ term does not alter the velocity magnitude, we compute the Lorentz factor by first applying a kick to the particle velocity, $u_p^{*,-} = u_p^n + (h/2) c E^n$, and then compute

$$\gamma^{*,n} = \sqrt{1 + \left(\frac{u^{*,-}}{\mathbb{C}} \right)^2}. \qquad (36)$$

Equation (35) can then be solved to obtain

$$u_p^{*,n} = (I - M^{*,n})^{-1} u_p^{*,-}, \qquad (37)$$

where

$$(I - M^{*,n})_{ij}^{-1} = \frac{\delta_{ij} + b_i b_j - M_{ij}^{*,n}}{1 + b^2}, \qquad (38)$$

with $M = I \times b$ and $b = (h/2) B^{*,n}/\gamma^{*,n}$. The value of the magnetic field is interpolated at the particle position using the half-time step magnetic field $B^{n+\frac{1}{2}}$ already available from the MHD integrator.

After the predictor step, the full electric field can be evaluated using Equation (15), and the particle positions and velocities can be restored to their initial values x_p^n and v_p^n. Note that since only an approximate value of the solution is needed, we do not apply a cleaning step to make E and B orthogonal during the predictor step. We point out that the predictor step is only used to predict the half-time level approximation to the electromotive force but not for the actual evolution of the CR particles, which are advanced according to the Boris pusher, Equation (31).

3.2.2. Particle Subcycling

At large energies, the particle evolution timescale can become considerably shorter than the fluid dynamical time, slowing down the total computational time. To overcome this issue, we allow multiple particle time steps to be taken during a single fluid update. Our approach improves over that of Bai et al. (2015) in several aspects.

Let N_{sub} be the number of steps involved during the subcycling. The particle pusher Equation (31) is now applied N_{sub} times over equally spaced time intervals $[t^{n+\theta k}, t^{n+\theta(k+1)}]$ of length $\theta \Delta t$, where $\theta = 1/N_{sub}$ and $k = 0,...,N_{sub} - 1$. During subcycling, electric and magnetic fields are kept constant at the predicted half-time level with the exception of the CR-Hall term (the second term in Equation (15)), which is recomputed in order to maintain second-order accuracy.

We elaborated two forms of subcycling, taking advantage of the momentum and energy deposition (needed for feedback) accumulated at each fluid step.

1. The first strategy recomputes the force at each substep and can be used with an even or odd number of steps.
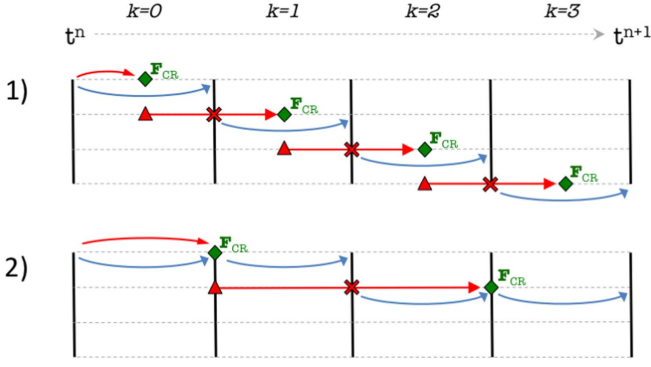
Figure 1. Subcycling methods 1 (top) and 2 (bottom) for $N_{sub} = 4$. Blue arrows represent the application of the Boris pusher; red triangles (momentum variation) and crosses (direct computation of the CR force) joined by a red line are used to extrapolate $\boldsymbol{F}_{CR}$ at the next half substep (green diamonds, method 1) or full substep (green diamonds, method 2). The curved red line at the beginning of the cycle represents the application of the predictor step.

After solution values have evolved to the intermediate level $(\boldsymbol{x}_p, \boldsymbol{v}_p)^{n+\theta k}$, we recompute the CR force using Equation (14), correct the electric field using Equation (15), and for $k > 0$, predict the midpoint force value for the next substep using time extrapolation:

$$\boldsymbol{F}_{CR}^{n+\theta(k+\frac{1}{2})} = 2\boldsymbol{F}_{CR}^{n+\theta k} - \left(\frac{\Delta \boldsymbol{m}}{\theta \Delta t}\right)^{n+\theta(k-\frac{1}{2})}, \qquad (39)$$

where $\Delta \boldsymbol{m}^{n+\theta(k-\frac{1}{2})}$ is the momentum difference over the previous subcycle. At the beginning of the cycle $(k = 0)$, we employ the predictor step given by Equation (37) with $\theta \Delta t/2$. This method is represented in the top panel of Figure 1.

2. The second strategy recomputes the electric field every other substep, thus leading to a more efficient scheme that can be used with an even number of substeps. The electric field is extrapolated in time (when $k = 2, 4, 6, \ldots$) by a full substep by taking advantage of the total momentum variation accumulated until then,

$$\boldsymbol{F}_{CR}^{n+\theta(k+1)} = \frac{k + 2}{k} \boldsymbol{F}_{CR}^{n+\theta k}$$
$$- \frac{2}{k}\left(\frac{1}{k\theta\Delta t}\sum_{j=1}^{k}\Delta \boldsymbol{m}^{n+\theta(j-\frac{1}{2})}\right), \qquad (40)$$

where the summation represents the total momentum change accumulated over k substeps. Note that when k is odd, we do not recompute $\boldsymbol{F}_{CR}$.

At the beginning of the cycle $(k = 0)$, we employ the predictor step given by Equation (37) with the time step $\theta \Delta t$. This method is represented in the bottom panel of Figure 1 in the case where $N_{sub} = 4$.

3.3. Connection between Grid and Particle Quantities

An important step of the algorithm requires depositing particle quantities to the grid and interpolating fluid quantities at the particle locations.

Let q_p be a quantity associated with a particle (e.g., charge or velocity), then the deposition in cell (i, j, k) is achieved by a weighted sum,

$$Q_{ijk} = \sum_{p=1}^{N_p} W(\boldsymbol{x}_i - \boldsymbol{x}_p)q_p, \qquad (41)$$

where $W(\boldsymbol{x}_i - \boldsymbol{x}_p) = W(x_i - x_p)W(y_j - y_p)W(z_k - z_p)$ is the product of three one-dimensional weight functions. Within PLUTO, we have implemented traditional shape functions such as the "Nearest Neighbor Point" (NGP), "Cloud-In-Cell" (CIC), and "Triangular Shape Cloud" (TSC). The explicit formula for the weight can be found, e.g., in Haugbølle et al. (2013). In practice, since the weight functions have a finite stencil that extends over three zones, each particle can give a nonzero contribution only to the computational zone hosting the particle, its left and right neighbors. If $\delta = (x_p - x_i)/\Delta x$ is the distance between the particle and the ith zone such that $\delta \in [-1/2, 1/2]$, the corresponding weights W_i, W_{i-1}, and W_{i+1} are computed as

1. Nearest grid point (NGP):

$$W_{i\pm 1} = 0; \quad W_i = 1; \qquad (42)$$

2. Cloud-in-cell (CIC):

$$W_{i\pm 1} = \frac{|\delta| \pm \delta}{2}; \quad W_i = 1 - |\delta|; \qquad (43)$$

3. Triangular Shape Cloud (TSC):

$$W_{i\pm 1} = \frac{1}{2}\left(\frac{1}{2} \pm \delta\right)^2; \quad W_i = \frac{3}{4} - \delta^2; \qquad (44)$$

Note that $W_{i-1} + W_i + W_{i+1} = 1$ when $\delta \in [-1/2, 1/2]$.

Particle interpolation (also referred to as field weighting) is the opposite process of interpolating grid (fluid) quantities at a given particle position:

$$q_p = \sum_{ijk} W(\boldsymbol{x}_{ijk} - \boldsymbol{x}_p)Q_{ijk}, \qquad (45)$$

where only neighbor cells give a nonzero contribution to the particle. For consistency, the same weighting scheme must be used for particles and field (see Birdsall & Langdon 2004).

4. Numerical Benchmarks and Code Performance

In this section, we present selected numerical benchmarks in order to verify the correctness and accuracy of our MHD–PIC and test-particle model implementations.

Before proceeding, we point out that while the ideal MHD equations are notoriously scale invariant, the presence of nonzero source terms on the right-hand side of the momentum and energy equations, Equations (4) and (6), breaks down this property. If we denote with L_0, ρ_0, and V_0 our physical reference units for length, density, and velocity (respectively), a straightforward analysis shows that the source terms (and similarly the particle equation of motion (17)) are rescaled by a factor $L_0\omega_{pi}/c$, where ω_{pi} is the ion plasma frequency. This naturally suggests the ion skin depth c/ω_{pi} as the natural reference length. In addition, if the Alfvén velocity v_A is used as the reference speed, time will be conveniently expressed in units of the inverse Larmor frequency $\Omega_L^{-1} = c/(\omega_{pi}v_A)$.

4.1. Particle Gyration

We begin by considering the gyration of a single test particle in a constant magnetic field directed along the vertical axis, $\boldsymbol{B} = (0, 0, B_0)$. Fluid backreaction is not included as in Bai et al. (2015). We solve the MHD–PIC equations in a reference frame Σ where the background fluid has constant density and pressure as it is uniformly advected in the x direction with velocity $\boldsymbol{v}_g = (V_g, 0, 0)$.

The motion of the particle is more conveniently described in the fluid comoving frame Σ', where the inductive electric field vanishes and the particle equation of motion reduces to

$$\frac{d(\gamma'_p \boldsymbol{v}'_p)}{dt'} = \alpha_p \boldsymbol{v}'_p \times \boldsymbol{B}' , \tag{46}$$

where the primed quantities are now in the fluid rest frame. The general solution of Equation (46), for a point charge located at the origin of Σ', is a simple gyration:

$$\begin{cases} x'_p(t) = \frac{v'^{\,0}_{p,x} \sin(\Omega' t') + v'^{\,0}_{p,y}[1 - \cos(\Omega' t')]}{\Omega'} \\ y'_p(t) = \frac{v'^{\,0}_{p,x}[\cos(\Omega' t') - 1] + v'^{\,0}_{p,y} \sin(\Omega' t')}{\Omega'} \\ v'_{x,p}(t) = v'^{\,0}_{p,x} \cos(\Omega' t') + v'^{\,0}_{p,y} \sin(\Omega' t') \\ v'_{y,p}(t) = -v'^{\,0}_{p,x} \sin(\Omega' t') + v'^{\,0}_{p,y} \cos(\Omega' t') \end{cases} , \tag{47}$$

where $v'^{\,0}_{x,p}$ and $v'^{\,0}_{y,p}$ are the Cartesian components of the particle initial velocity $\boldsymbol{v}'_p$ while

$$\Omega'_L = \frac{\alpha_p B'_0}{\gamma'_p}, \qquad B'_0 = B_0 \sqrt{1 - \left(\frac{V_g}{\mathbb{C}}\right)^2} \tag{48}$$

are the Larmor gyrofrequency and magnetic field in the Σ' frame. The gyration radius is $R'_L = v'_p / \Omega'$, and the particle kinetic energy must be conserved in this frame, i.e.,

$$E'_{k,p} = (\gamma'_p - 1)\mathbb{C}^2 = \text{const.} \tag{49}$$

For the present test, we prescribe $\boldsymbol{v}'_p = (0, u'_p / \gamma'_p, 0)$, where u'_p is the particle four-velocity and $\gamma'_p = \sqrt{1 + (u'_p / \mathbb{C})^2}$ its Lorentz factor, and we set $\mathbb{C} = 10$ and $\alpha_p = B_0 = 1$. Velocity components in the lab frame are easily found through a Lorentz transformation. Following Bai et al. (2015), we consider both nonrelativistic ($u'_p = 1$) and relativistic ($u'_p = 100$) test particles, with or without drift velocity.

In order to mimic the variable time step generally expected in fluid simulations, we set the time step to be $\Delta t = \Delta t_0 (1 + 0.2 \cos \varphi)$, where φ is a random number in the range $[0, 2\pi]$ and $\Delta t_0 = 0.5$ (nonrelativistic particle) or $\Delta t_0 = 5$ (relativistic particle). With this choice, $\Omega'_L \Delta t \approx 0.5$ in both cases. Particle subcycling is not employed. As pointed out in Bai et al. (2015), a relatively large time step has been chosen to amplify the error.

Nonrelativistic Particle. In the top panels of Figure 2, we plot, in the comoving frame, the energy (left) and y' coordinate (right) as a function of time for a nonrelativistic particle with $u'_p = 1$ and $V_g = 0$ (no drift, blue dashed line) or $V_g = 1$ (drift, red dashed line). The particle's initial energy in the comoving frame is therefore $E'_{k,p} \approx 0.4988$ while its gyration radius is $R'_L = 1$. Energy is conserved exactly in the absence of drift, while it shows small-amplitude oscillations corresponding to a relative error of $\approx 0.1\%$ when $V_g = 1$. Phase errors are also

within an acceptable level, and results are in good agreement with those of Bai et al. (2015).

Relativistic Particle. In the bottom panels of Figure 2, we show the evolution of a test particle with initial velocity $u'_p = 100$ ($\gamma'_p \approx 10$). In this case, $\Omega' \approx 0.1$, and we set $\Delta t_0 = 5$ so that $\Delta t_0 \Omega'_L = 0.5$ as in the previous case. From Equation (49), we have $E'_{k,p} \approx 904.99$ while the gyration radius is $R'_L = 100$. Exact energy conservation is achieved during the evolution in the absence of drift, while small-amplitude oscillations are present when $V_g = 1$. The relative errors are $\lesssim 0.05\%$, slightly less than before. Phase errors are comparable to those in the nonrelativistic case.

Our results agree well with those of Bai et al. (2015). We conclude that, since in most astrophysical applications $\Omega_L \Delta t < 0.5$, we can safely depend on our implementation of the Boris algorithm.

4.2. Particle Motion in Non-orthogonal Electric and Magnetic Fields

Next, we consider the motion of a relativistic charged particle in non-orthogonal electric and magnetic fields.

The initial condition consists of a spatially uniform plasma with constant density and pressure with $\boldsymbol{E} = (0, E_y, E_z)$, $\boldsymbol{B} = (0, 0, B_z)$. The fluid is assumed to be at rest. A single test particle is initially placed at the origin, with the velocity along the x axis, i.e., $\boldsymbol{v}_p(0) = v_0 \hat{\boldsymbol{e}}_x$.

This problem has an exact solution that is best expressed in a frame of reference where the electric and magnetic fields are parallel (Landau & Lifshitz 1975) through a Lorentz boost with velocity

$$\frac{\boldsymbol{V}}{c} = \frac{\boldsymbol{E}^2 + \boldsymbol{B}^2 - \sqrt{(\boldsymbol{E}^2 - \boldsymbol{B}^2)^2 + 4(\boldsymbol{E} \cdot \boldsymbol{B})^2}}{2|\boldsymbol{E} \times \boldsymbol{B}|^2}(\boldsymbol{E} \times \boldsymbol{B}). \tag{50}$$

In this frame, the electric and magnetic fields become parallel with components $\tilde{\boldsymbol{E}} = (0, \tilde{E}_y, \tilde{E}_z)$ and $\tilde{\boldsymbol{B}} = (0, \tilde{B}_y, \tilde{B}_z)$. A rotation is then performed in order to place the electric (and thus the magnetic) field along the z axis:

$$\begin{pmatrix} E'_y \\ E'_z \end{pmatrix} = \begin{pmatrix} \cos\theta & \sin\theta \\ -\sin\theta & \cos\theta \end{pmatrix} \begin{pmatrix} \tilde{E}_y \\ \tilde{E}_z \end{pmatrix}, \tag{51}$$

where $\theta = \arctan(-\tilde{E}_y / \tilde{E}_z)$. In the Σ' frame, it is straightforward to show that the particle initial velocity is still directed along the x' direction. The solution of Equation (17) for a charged particle located at the origin of Σ' (Landau & Lifshitz 1975) can be written in terms of perpendicular components,

$$\boldsymbol{x}'_{p,\perp}(t') = \frac{v'_0}{\Omega'_L}[\sin\phi(t'), \cos\phi(t') - 1, 0]$$

$$\boldsymbol{v}'_{p,\perp}(t') = \frac{v'_0}{\Omega'_L}[\cos\phi(t'), -\sin\phi(t'), 0]\frac{d\phi}{dt'}, \tag{52}$$

and parallel components

$$\begin{cases} z'_p(t') &= c\tau_E \cosh\left(\frac{E'}{B'}\phi(t')\right) \\ v'_{z,p}(t') &= \frac{c}{\Omega'_L} \sinh\left(\frac{E'}{B'}\phi(t')\right)\frac{d\phi}{dt'} . \end{cases} \tag{53}$$

In the above expressions, $E' \equiv E'_z$ while Ω'_L and τ_E are the gyrofrequency and the acceleration timescale in the Σ' frame
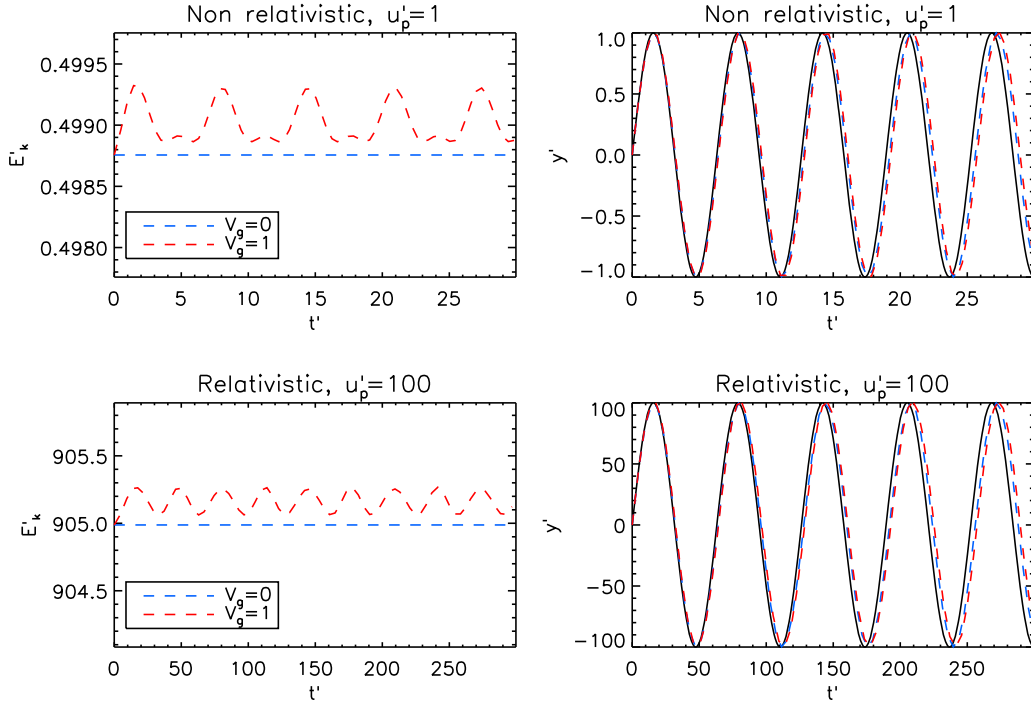
Figure 2. Particle kinetic energy (left panels) and position (right panels) as a function of time for the gyration test problem. Quantities are plotted in the fluid rest frame. The top and bottom panels show, respectively, the results for a nonrelativistic ($u_p' = 1$) and relativistic ($u_p' = 100$) test particle. Blue and red dashed lines correspond, respectively, to zero background flow velocity ($V_g = 0$) and mildly relativistic flow ($V_g = 1$).

defined, respectively, as

$$\Omega_L' = \frac{\alpha_p B'}{\gamma_0'}, \qquad \tau_E = \frac{1}{\alpha_p E'}. \qquad (54)$$

Finally, $\phi(t')$ is given by

$$\phi(t') = \frac{B'}{E'}\text{arcsinh}\left(\frac{c^2}{E_{k0}'}\frac{t'}{\tau_E}\right), \qquad (55)$$

where $E_{k0}' = (\gamma_0' - 1)c^2$ represents the initial particle kinetic energy (per unit mass). Notice that our solution has been derived under the assumption that the particle initial velocity lies in the x direction only.

Equations (52) and (53) describe a stretched helical trajectory with an exponentially increasing pitch. Note that t' is the time coordinate in the Σ' frame.

For the present test, we prescribe $\boldsymbol{v}_p(0) = (0.5, 0, 0)$, $\boldsymbol{E} = (0, 0.3, 0.5)$, and $\boldsymbol{B} = (0, 0, 1)$, and set the charge to mass ratio as well as the artificial speed of light $\mathbb{C}$ equal to 1. We integrate the particle equation of motion until $t_s = 200$, and as in the previous test, we set the time step to be $\Delta t = \Delta t_0(1 + 0.2\cos\varphi)$, where φ is a random number between 0 and 2π, and $\Delta t_0 = 0.5$. Particle subcycling is not employed.

In the top panels of Figure 3, we plot, in the Σ' frame, the x coordinate (left panel) and the y coordinate (right panel) as a function of time for a relativistic particle in a generic electromagnetic field. Likewise, we plot, in the bottom panels, the z component of the velocity (left panel) and the particle energy (right panel). The relative error is computed by transforming the energy in the Σ' frame and then taking the

maximum value over time:

$$\Delta_{L1} = \max\left[\frac{|E_{k,p}'(t'^n) - E_{k,p}'^{\text{ex}}(t'^n)|}{E_{k,p}'^{\text{ex}}(t'^n)}\right], \qquad (56)$$

where $E_{k,p}' = (\gamma' - 1)\mathbb{C}^2$ is the particle (specific) kinetic energy while

$$E_{k,p}'^{\text{ex}}(t') = \mathbb{C}^2\sqrt{(\gamma_0')^2 + \left(\frac{t'}{\tau_E}\right)^2} - \mathbb{C}^2 \qquad (57)$$

is the exact expression for the particle energy as a function of time. We obtain $\Delta_{L1} \lesssim 0.1\%$, showing good agreement between the analytic and numerical solutions.

4.3. Fluid–Particle Relative Drift

We now assess the temporal accuracy of our integration schemes by considering the evolution of the full gas–CR system starting from a spatially uniform distribution of gas and particles. The computational domain is a doubly periodic 2D box defined by $x, y \in [-1, 1]$ with constant magnetic field and orthogonal to the plane of computation, $\boldsymbol{B} = (0, 0, B_0)$. We choose a frame of reference where the total (gas+CR) momentum is zero so that, at $t = 0$, gas and particles stream in opposite directions,

$$\boldsymbol{v}_g(0) = -\frac{\varrho_p}{\rho}v_0\hat{\boldsymbol{e}}_x, \qquad \boldsymbol{v}_p(0) = v_0\hat{\boldsymbol{e}}_x. \qquad (58)$$

The density and pressure of the fluid are set to unity. The evolution of the composite (gas + particles) system, which now includes CR feedback, is governed by the MHD–PIC Equations (3)–(6), which, in the absence of spatial gradients,
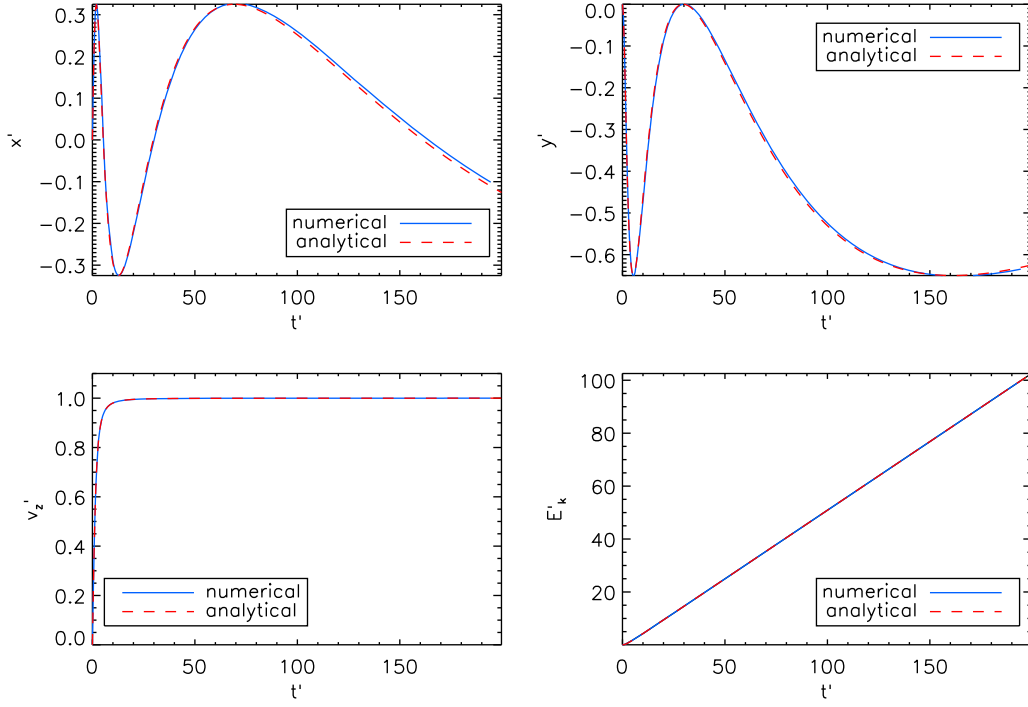
Figure 3. Particle position (top panels), velocity (bottom-left panel), and energy density (bottom-right panel) as a function of time for a charged particle in generic electric and magnetic fields. Quantities are plotted in the frame where both electric and magnetic fields are along the z axis.

reduce to

$$\begin{cases} \dfrac{d\boldsymbol{v}_g}{dt} = \alpha_i R(\boldsymbol{v}_g - \boldsymbol{v}_p) \times \boldsymbol{B} \\ \dfrac{d\boldsymbol{v}_p}{dt} = \alpha_p(1 - R)[(\boldsymbol{v}_p - \boldsymbol{v}_g) \times \boldsymbol{B}] \end{cases}, \qquad (59)$$

where α_i and α_p denote, as usual, the charge to mass density ratios of the ions and the CR particles, respectively. Note that in writing Equation (59) we have tacitly assumed that $\boldsymbol{v}_p \equiv \boldsymbol{v}_{CR}$ in the absence of spatial dependence. Also, the expression for the CR force appearing on the right-hand side of Equation (4) has been rewritten by combining Equation (15) with the $\boldsymbol{E}$ given by Equation (12), yielding

$$\boldsymbol{F}_{CR} = \frac{q_i}{c} R(\boldsymbol{v}_{CR} - \boldsymbol{v}_g) \times \boldsymbol{B}. \qquad (60)$$

The system of ordinary differential equations (59) with the initial conditions previously specified has an exact analytic solution given by

$$\begin{cases} \boldsymbol{v}_g^{ex}(t) = -\dfrac{\Omega_g}{\Omega_p}\boldsymbol{v}_p^{ex}(t) \\ \boldsymbol{v}_p^{ex}(t) = v_0[\cos(\Omega t)\hat{\boldsymbol{e}}_x - \sin(\Omega t)\hat{\boldsymbol{e}}_y] \end{cases}, \qquad (61)$$

where $\Omega = \Omega_g + \Omega_p$, $\Omega_g = \alpha_i R B_0$, and $\Omega_p = \alpha_p(1 - R)B_0$. Note also that from the definition of $R = \alpha_p \varrho_p / (\alpha_i \rho_i + \alpha_p \varrho_p)$, we have $\rho\Omega_g = \varrho_p\Omega_p$. Equation (61) shows that both particles and gas trace clockwise circular orbits with the same period but different radii. It can also be easily verified that the total (gas +particle) momentum remains constant in time, as expected.

We choose $\alpha_p = \alpha_i = 1$ and $B_0 = 2\pi$ so that our units are such that $\Omega = 2\pi$. For the test considered here, we set $v_0 = 5$ and $\varrho_p = 10^{-2}\rho$. We use 8×8 grid zones and one particle per

cell. The system is evolved for exactly one period $T = 1$ using constant time steps $\Delta t = 1/N_t$, where N_t is the number of (fluid) time steps: $N_t = 40, 80, 160,..., 81920$. For the sake of comparison, we have repeated computations with and without the predictor step (see Section 3.2.1) and also by varying the number of substeps used during particle subcycling. Both subcycling methods, illustrated in Section 3.2.2, have been compared with $N_{sub} = 1$ and $N_{sub} = 5$ ($N_{sub} = 4$ for method 2). The error is computed at the end of each computation using the L_1 norm,

$$\Delta_{L1} = |\boldsymbol{v}_g(T) - \boldsymbol{v}_g^{ex}(T)| + |\boldsymbol{v}_p(T) - \boldsymbol{v}_p^{ex}(T)|, \qquad (62)$$

and it is plotted in Figure 4 without subcycling (left panel, $N_{sub} = 1$) and with subcycling (right, $N_{sub} > 1$).

Results obtained without the predictor step (labeled with "np," red plus signs) show essentially first-order accuracy regardless of subcycling ($N_{sub} = 1$ or $N_{sub} = 5$ in the left and right panels, respectively). On the contrary, including the predictor step noticeably improves the overall scheme's convergence, yielding genuine second-order temporal accuracy. This holds when $N_{sub} = 1$ (left panel) and also when $N_{sub} > 1$ (right panel). Results obtained with subcycling methods 1 and 2 are both reported using the blue triangles and green crosses in Figure 4 and labeled, respectively, with "wp1" and "wp2". Notice that while method 1 can be used for any $N_{sub} \geqslant 1$ (we employ $N_{sub} = 5$), method 2 works only when N_{sub} is even (we set $N_{sub} = 4$).

Note that computations have been carried out using both the CTU and RK2 time-stepping methods, and the results are identical. Indeed, in the absence of spatial gradients, the two methods become coincident as it can be easily verified from Equations (26) and (30) with $\mathcal{L} = 0$.

9
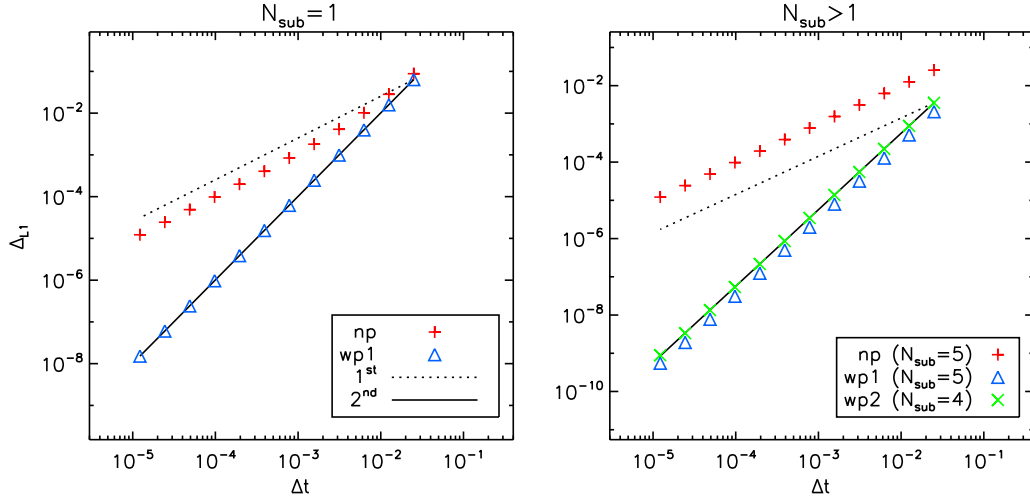
Figure 4. L_1 norm errors for the fluid–particle relative drift problem using the standard particle update without subcycling (left panel) and with subcycling (right panel). Results after one period obtained without the predictor step (np) are shown using red plus signs while blue triangles and green crosses correspond to computations obtained by including the predictor step with either subcycling methods 1 (wp1) or 2 (wp2); see Section 3.2.2. Computations using subcycling employ $N_{sub} = 5$ except for subcycling method 2, for which we set $N_{sub} = 4$. The black dashed (solid) line gives the expected convergence rate for a first-order (second-order) temporally accurate scheme.

4.4. Nonresonant Bell Instability

In the next test, we verify the implementation of our MHD–PIC module by investigating the linear growth of the nonresonant Bell instability (Bell 2004) in one, two, and three dimensions. The instability is driven by the relative streaming between gas and CR particles along magnetic field lines, and it takes place when the CR drift velocity exceeds the local Alfvén speed. The streaming of CRs generates a return current in the thermal plasma (in the attempt to restore charge neutrality), so that small perturbations are amplified when the induced Lorentz force exceeds the magnetic tension. The instability excites nearly purely growing modes with wavelengths shorter than the Larmor radius and does not saturate when $\delta \boldsymbol{B}/\boldsymbol{B} \sim 1$, but it continues growing to produce amplified magnetic fields much larger than the initial field (Bell 2013). This mechanism is believed to operate in the upstream regions of high Mach number SNR shocks, leading to efficient magnetic field amplification and the development of turbulence. Magnetic field fluctuations in the upstream magnetic field are then responsible for the scattering of CRs and their confinement close to the shock front (Bell 2004; Bai et al. 2015), thereby providing an efficient mechanism to trigger diffusive shock acceleration.

Bai et al. (2015) have carried out a linear stability analysis by including the CR-Hall term that was previously ignored. The quantity

$$\Lambda = R \frac{|v_{CR} - v_g|}{v_A}, \quad (63)$$

where v_A is the Alfvén velocity, determines the importance of the CR-Hall term and leads essentially to a reduction of the growth rate, which saturates at the ion cyclotron frequency of the background plasma when J_{CR} is increased, in the limit $\Lambda \gg 1$.

Here we consider the opposite limit ($\Lambda \ll 1$), which is also the same regime used in Bell (2004; regime II). Assuming incompressible perturbations proportional to $e^{i(kx-\omega t)}$ in the

fluid rest frame, the dispersion relation becomes

$$\frac{\omega(k)}{k_0 v_A} = \epsilon + \sqrt{\left(\frac{k}{k_0}\right)^2 - 2\frac{k}{k_0} + \epsilon^2}, \quad (64)$$

where $\epsilon = v_A/v_{CR}$ and

$$k_0 = \frac{J_{CR}}{2B_0 c} \quad (65)$$

is the most unstable wavenumber with $\boldsymbol{J}_{CR} = e n_{CR} \boldsymbol{v}_{CR}$ the CR current density. The maximum growth rate is obtained when $k = k_0$, yielding

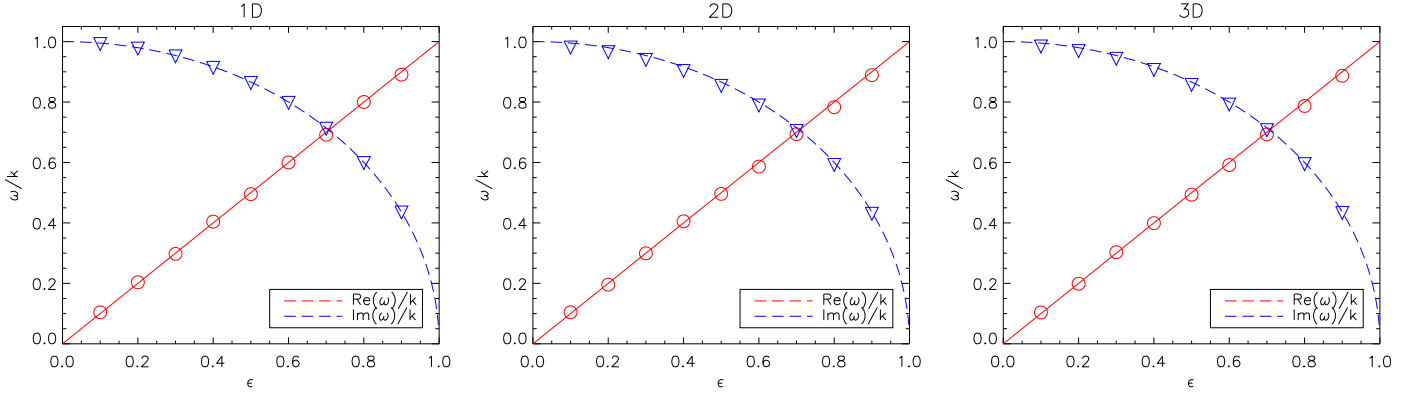$$\omega_0 = k_0 v_A (\epsilon + i\sqrt{1 - \epsilon^2}). \quad (66)$$

To set up the problem, we consider a periodic box $x \in [0, L_x]$, $y \in [0, L_y]$, and $z \in [0, L_z]$ initially filled with a plasma with uniform density and pressure (we set $\rho = 1$, $p = 1$) and threaded by a constant background magnetic field $\boldsymbol{B}_0 = (1, 0, 0)$. A monochromatic beam of CR particles is set to travel along the x direction with velocity $v_{CR} = v_A/\epsilon$, where $\epsilon \in (0, 1)$ is now a free parameter. In order to ensure that the CR current remains constant during the evolution, particles must have a large inertia, and this is achieved by setting the charge to mass ratio of CR particles to be very small, i.e., $\alpha_p = 10^{-6} v_A k_0/B_0$. Using the definition of the CR current together with Equation (65) for the most unstable wavenumber, one obtains that the CR density satisfies $\varrho_p = 2 \times 10^6 \epsilon B_0^2/v_A^2$. Finally, to ensure that $R \ll 1$, we set $\alpha_i = 10^3$ while the speed of light is fixed to $\mathbb{C} = 10^6$.

Perturbations in velocity and magnetic field at $t = 0$ are introduced by using the exact eigenvectors obtained from the 1D linear dispersion relation in the limit $\Lambda = R v_{CR}/v_A \ll 1$ (see the appendix to Bai et al. 2015) according to which

$$\delta \boldsymbol{v}_g = v_A \frac{b_\perp}{B_0} [0, \cos(\phi - \theta), \sin(\phi - \theta)] \quad (67)$$

and

$$\delta \boldsymbol{B} = b_\perp [0, \cos(\phi), \sin(\phi)], \quad (68)$$

Figure 5. Real (red) and imaginary (blue) parts of the growth rate for the nonresonant Bell instability problem using different values of the ϵ parameter. The solid and dashed lines give the theoretical expectation, Equation (66), while the symbols (triangles and circles) are the results measured from the simulations using the CTU scheme.

where $\phi = k_0 x$, $\theta = \sin^{-1}\epsilon$, and $b_\perp = 10^{-5}$ is the initial perturbation amplitude.

In 1D, we set $k_0 = 2\pi$ so that, by choosing the box size $L_x = 1$, we fit exactly one wavelength (the most unstable) in the computational domain. In 2D and 3D, the initial configuration is rotated so that the new wavevector is not grid aligned but has the orientation

$$\boldsymbol{k}_0' = \frac{2\pi}{L_x}(1, \tan\alpha, \tan\beta), \qquad (69)$$

where $\tan\alpha = L_x/L_y$ and $\tan\beta = L_x/L_z$ still satisfy $|\boldsymbol{k}_0'| = 2\pi$. Vectors are then rotated using $\boldsymbol{v}_g' = \mathsf{R}_{\gamma\alpha}\delta\boldsymbol{v}_g$ and $\boldsymbol{B}' = \mathsf{R}_{\gamma\alpha}(\boldsymbol{B}_0 + \delta\boldsymbol{B})$, where the rotation matrix $\mathsf{R}_{\gamma\alpha}$ is defined as (see also, e.g., Mignone & Tzeferacos 2010)

$$\mathsf{R}_{\gamma\alpha} = \begin{pmatrix} \cos\alpha\cos\gamma & -\sin\alpha & -\cos\alpha\sin\gamma \\ \sin\alpha\cos\gamma & \cos\alpha & -\sin\alpha\sin\gamma \\ \sin\gamma & 0 & \cos\gamma \end{pmatrix}, \qquad (70)$$

where $\tan\gamma = \cos\alpha\tan\beta$. In 2D, we employ $L_x = 2L_y = \sqrt{5}$ using 64×32 zones while in 3D, we set $L_x = 2L_y = 2L_z = 3$ using $96 \times 48 \times 48$ zones. We run nine simulations corresponding to $\epsilon = 0.1,\ldots,0.9$ for each case. For the sake of comparison, we perform computations using the CTU scheme with a MUSCL-Hancock predictor step and the RK2 scheme. The CFL number is set to 0.45 except for the 3D run using the Runge–Kutta scheme, for which we lower it to 0.3.

In order to measure the growth rate, we first evaluate, at each time t, the transverse magnetic energy as $p_{m\perp} = (\mathsf{R}_{\gamma\alpha}^{-1}\boldsymbol{B}' - \boldsymbol{B}_0)^2/2$ and then find the value t_{max} at which a maximum is reached. The imaginary part is then computed as the difference between $p_{m\perp}$ at $t_e = 3t_{max}/4$ and $t_b = t_{max}/4$:

$$\text{Im}(\omega) = \frac{1}{t_e - t_b}\log\left[\frac{p_{m\perp}(t_e)}{p_{m\perp}(t_b)}\right]. \qquad (71)$$

Likewise, we compute the real part by measuring the distance traveled by a wave crest from t_e to t_b:

$$\text{Re}(\omega) = k_x\frac{x_{max}(t_e) - x_{max}(t_b)}{t_e - t_b}, \qquad (72)$$

where $x_{max}(t_b)$ denotes the horizontal position of the first maximum of the z component of $\boldsymbol{B}_\perp' = \boldsymbol{B}' - (\boldsymbol{k}\cdot\boldsymbol{B})\boldsymbol{k}/k_0^2$.

Results obtained with the CTU and RK2 schemes are shown, respectively, in Figures 5 and 6, where we plot, from left to right, the real and imaginary parts of the growth rate (red and blue symbols) together with their analytic values (red and blue lines) as given by Equation (66) in 1D, 2D, and 3D, respectively. Our results show a good agreement with the analytic predictions, and a quantitative analysis shows that the relative error computed as

$$\Delta = \max_\epsilon\left(\left|\left|\frac{\omega(\epsilon)}{\omega_0(\epsilon)} - 1\right|\right|\right) \qquad (73)$$

never exceeds $\sim 4\%$ for the real part and $\sim 1.5\%$ for the imaginary part. In Equation (73), $\omega(\epsilon)$ refers to the (real or imaginary part of the) measured value of the growth rate while $\omega_0(\epsilon)$ is given by Equation (66). Error values are reported in Table 1 for the CTU and RK2 schemes in one, two, and three dimensions.

4.5. Application to Collisionless Shocks

In this section, we apply our MHD–PIC module to investigate particle (ion) acceleration in parallel MHD collisionless shocks. Our configuration reproduces the setup described by Bai et al. (2015) in their R2 (classical) and R2-REL (relativistic) fiducial computations. Note that while the fluid is always described by the classical MHD equations, the two runs differ essentially for the reduced speed of light ($\mathbb{C} = 10^4$ and $\mathbb{C} = 10\sqrt{2}\,v_0$, respectively).

The computational box is defined by the 2D rectangular domain with $0 \leqslant x \leqslant L_x$ and $0 \leqslant y \leqslant L_y$, where $(L_x, L_y) = (120, 3) \times 10^3$ for run R2 while a larger box $(L_x, L_y) = (384, 4.8) \times 10^3$ is used for the relativistic case (run R2-REL). Lengths are conveniently expressed in units of the ion skin depth c/ω_{pi}. The initial condition consists of a constant density and pressure ($\rho_0 = 1$, $p_0 = 1$) supersonic inflow propagating to the left with velocity $v_0 = -M_A$, where $M_A = 30$ is the Alfvénic Mach number. An ideal equation of state with the specific heat ratio $\gamma = 5/3$ is employed. The magnetic field is initially constant and parallel to the flow velocity $\boldsymbol{B} = (B_0, 0, 0)$. We set $B_0 = 1$ so that velocities will be normalized to the initial upstream Alfvén speed. This also sets the time unit as the inverse of the cyclotron frequency, $\Omega_L^{-1} = c/(\omega_{pi}v_A)$.
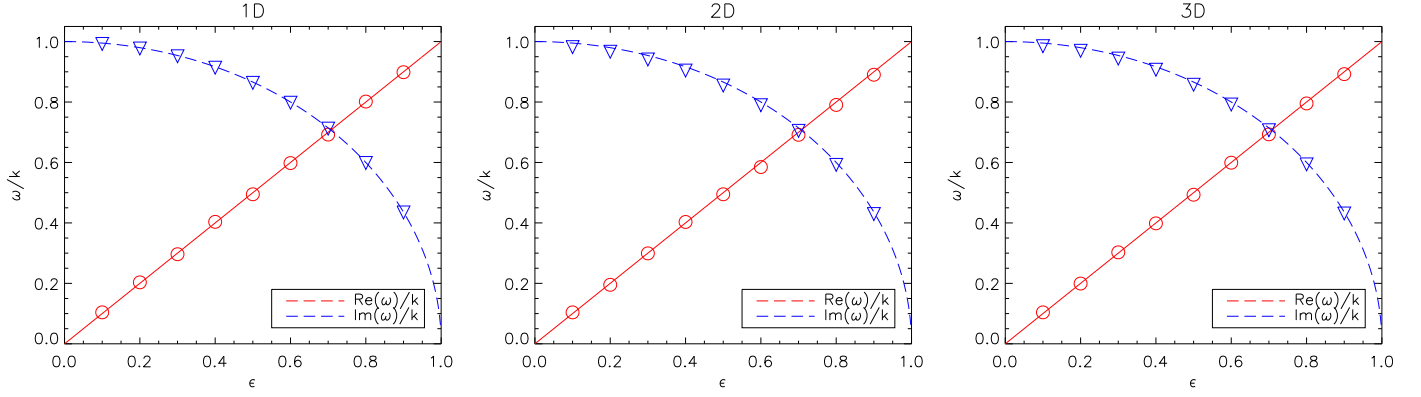
Figure 6. Same as Figure 5, but for the RK2 time stepping.

Table 1
Relative Errors for the Bell Instability Problem

	CTU		RK2	
	$\Delta_{\mathrm{Re}(\omega)}$	$\Delta_{\mathrm{Im}(\omega)}$	$\Delta_{\mathrm{Re}(\omega)}$	$\Delta_{\mathrm{Im}(\omega)}$
1D	4.21E–02	3.60E–03	4.08E–02	3.22E–03
2D	4.29E–02	1.51E–02	3.97E–02	1.50E–02
3D	3.77E–02	1.15E–02	4.06E–02	1.09E–02

We employ a uniform grid resolution of $[N_x, N_y] = [11520, 288]$ and $[N_x, N_y] = [30720, 384]$ for the two cases, respectively. This choice corresponds to a mesh resolution of $\approx 10.4\, c/\omega_{pi}$ and $\approx 12.5\, c/\omega_{pi}$ per cell, therefore giving a significant efficiency gain when compared to hybrid codes that typically require finer grids ($\approx 2\, c/\omega_{pi}$) to properly describe the microphysics. At the leftmost boundary ($x = 0$), we apply conducting conditions so that a right-going shock receding from the wall forms immediately. Constant flow injection holds at the right boundary $x = L_x$ while vertical boundary conditions are periodic. The MHD–PIC equations are evolved until $t = 3000\, \Omega_L^{-1}$ in the nonrelativistic run (run R2) while computations are stopped at $t = 11520\, \Omega_L^{-1}$ for the relativistic case.

4.5.1. Injection Recipe

Since the MHD–PIC approach cannot consistently model the injection physics, a prescription that mimics the generation of suprathermal particles in the downstream region of the shock is necessary. As shown by Caprioli & Spitkovsky (2014a) and Caprioli et al. (2015), the ion distribution immediately behind the shock shows an intermediate region of particles with mildly nonthermal energies. Hybrid simulations indicate that the fraction of injected particles can be effectively parameterized by defining a threshold energy, E_{inj}, which marks the boundary between the thermal and nonthermal distributions, and the injection fraction η. While Bai et al. (2015) prescribe an injection recipe that is strictly one dimensional, we present here a different approach that can also be used in the context of multidimensional calculations.

Particles are injected at the end of an "accumulation" cycle ΔT_{acc} consisting of a finite number of hydro steps during which we track the amount of mass swept by the shock. To this end, we add to the MHD–PIC equations the evolution of a passive tracer $\mathcal{T}$ which is updated in the following way:

1. At the beginning of an accumulation cycle, we set $\mathcal{T}_i = 0$ for all zones $i = (i, j)$ in the computational domain.

2. For each time step in the computation, we initialize the tracer to 1 if a computational zone lies within a shock and then update $\mathcal{T}$ regularly using our conservative scheme.

The criterion for a zone i to be considered inside a shock demands (i) the divergence of fluid velocity to be negative and (ii) the normalized second derivative of pressure to exceed a certain threshold:

$$\begin{cases} \sum_{d=x,y} \hat{e}_d \cdot (v_{g,i+\hat{e}_d} - v_{g,i-\hat{e}_d}) < 0, \\ \sum_{d=x,y} \dfrac{|p_{i+\hat{e}_d} - 2p_i + p_{i-\hat{e}_d}|}{p_{i+\hat{e}_d} + 2p_i + p_{i-\hat{e}_d}} > \chi \end{cases}, \quad (74)$$

where $i = (i, j)$, $\hat{e}_x = (1, 0)$, and $\hat{e}_y = (0, 1)$, while we set the threshold $\chi = 0.2$. An additional measure is necessary to avoid tracking the formation of secondary small discontinuities ahead or behind the shock during the turbulent regime. We achieve this by selecting, among shocked zones, those with a large pressure jump:

$$\begin{cases} \min(p_{i+\delta}) < \chi_{\min}, \\ \max(p_{i+\delta}) > \chi_{\max}. \end{cases} \quad (75)$$

where $\delta = [-1 .. 1, -1 .. 1]$ spans all of the eight neighbor zones. In order to detect the primary shock, we use $\chi_{\min} = 15$ and $\chi_{\max} = 250$. The criteria for choosing $\chi_{\min}$ and $\chi_{\max}$ depend on the shock that one wishes to track. The details of the computation are not sensitive to their values, inasmuch as $\chi_{\min}$ ($\chi_{\max}$) is larger (smaller) than the upstream (downstream) pressure.

If conditions (74) and (75) are both satisfied, we consider the zone to lie within a shock and set a flag $f_i = 1$ ($f_i = 0$ otherwise).

3. The passive scalar is evolved by repeating step 2 until the following condition is met:

$$\sum_i (\rho_{\mathrm{sh}})_i > Q \sum_i (\rho \mathcal{T})_i, \quad (76)$$

where $\rho_{\mathrm{sh}} = \rho \mathcal{T}(1 - f)$, the summation extends to all computational zones, $Q = 0.8$ is a safety factor, and f is the current shock detector flag defined in step 2. Equation (76) marks the end of the accumulation cycle ΔT_{acc}, and the summation on the left-hand side represents the total mass (density) swept by the shock during this interval of time by excluding zones that are currently flagged, which would otherwise tend to overestimate the swept mass.

The reliability of our mass-tracking algorithm has been tested on the 1D unperturbed propagation of the shock
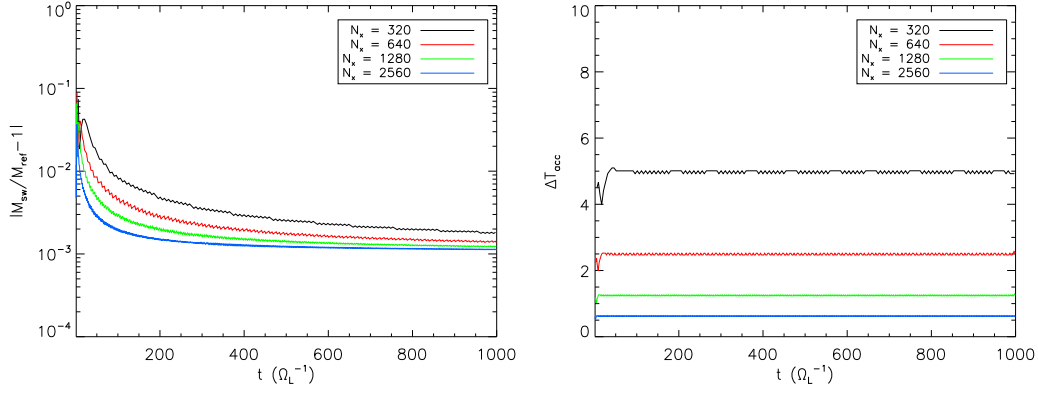
Figure 7. Left panel: relative error $|M_{sw}/M_{ref} - 1|$ of the cumulative swept mass as a function of time, where $M_{sw} = \Delta x \Delta y \int_0^t \sum_i (\rho_{sh})_i$ while $M_{ref} = \rho_0 v_{sh} t L_y$ is the expected value for a 1D plane-parallel shock. Right panel: duration of an accumulation cycle as a function of time. Colors correspond to different grid resolutions reported in the legend.

using different grid resolutions. Figure 7 shows (left panel) the relative error of the cumulative swept mass as a function of time: the uncertainty is larger at the beginning ($\approx 5\%$–10% due to start-up error and wall heating at the left boundary) while it progressively reduces to a few 10^{-3} at later times ($t \gtrsim 400\Omega_L^{-1}$). This error falls well within the uncertainty in estimating the mass fraction η ($\sim 10^{-3}$–10^{-4}; see Caprioli & Spitkovsky 2014a and the discussion below) of particles crossing the shock and participating in the DSA process. On the right-hand panel, we plot the duration of an accumulation cycle as a function of time and point out that our injection recipe is not continuous in time but, rather, occurs periodically with a period ΔT_{acc} that reduces as the mesh is refined. For the grid resolution employed here, the duration of a single accumulation cycle lasts approximately $\Delta T_{acc} \approx 2\Omega_L^{-1}$.

4. When condition (76) is fulfilled, particle injection takes place. The amount of CRs injected in each zone i is proportional to the local swept mass distribution, that is, $(N_{inj})_i = N_{\rho_0}(\rho_{sh})_i$ where $N_{\rho_0} = 4$ is the number of particles per cell at unit fluid density. Particles will be mostly injected into the shock downstream (where $\rho_{sh} \neq 0$), and their mass density is controlled by the parameter η such that $N_{inj}\varrho_p = \eta\rho_{sh}$. Following Bai et al. (2015), we set the CR mass fraction $\eta = 2 \times 10^{-3}$ (see also Section 3 of Caprioli & Spitkovsky 2014a for a thorough discussion) and therefore $\varrho_p = \eta/N_{\rho_0}$. As such, the mass of the injected particles is a fixed fraction η of the shock-swept mass.

Following Caprioli & Spitkovsky (2014a) and Caprioli et al. (2015), we set the energy of the injected particles to be $10E_{sh}$ in the comoving shock frame, where $E_{sh} = v_0^2/2$ is the shock-specific kinetic energy. In the lab frame, the particle velocity is therefore initialized to

$$\boldsymbol{v}_p = 10\hat{\boldsymbol{e}}_x + \sqrt{20E_{sh}} \begin{pmatrix} \sin\theta\cos\varphi \\ \sin\theta\sin\varphi \\ \cos\theta \end{pmatrix}, \qquad (77)$$

where θ and φ are randomly distributed angles.

Finally, the conservation of mass, momentum, and energy is enforced by subtracting the corresponding injected amount from the gas. This compensation procedure usually produces small variations, and test runs without it show negligible variations.

After the injection process has completed, the tracer $\mathcal{T}$ is again reset to zero everywhere and a new accumulation cycle begins (step 2).

Our injection prescription is independent of the shape and position of the shock front and as such, it can easily adapt to curved and corrugated fronts.

During the first phase of injection ($t \lesssim t_i = 480\,\Omega_L^{-1}$), CR streaming is effective only in triggering the onset of the Bell instability as turbulent fluctuations are still small. As pointed out by Bai et al. (2015), particles giving rise to this transient flow do not participate in the shock-acceleration process and are removed for $t > 2t_i$ in order to suppress spurious effects once the Bell instability is fully developed.

### 4.5.2. Nonrelativistic Regime

At the beginning, a shock is formed and reflected away from the wall at the left boundary. CR particles injected at this early stage travel almost undisturbed along magnetic field lines without being efficiently scattered and propagate away from the shock. The streaming of CRs in the upstream region triggers the Bell instability, which grows linearly for a few hundred Larmor periods. As the instability enters the nonlinear stage, magnetic field fluctuations are amplified by a factor of ~ 4 in the upstream region, and a filamentary-like structure, alternating between low- and high-density regions, becomes evident. Snapshots of the evolution, showing both density and magnetic field, are given in Figure 8. Note that only a smaller portion of the computation domain is shown. Magnetic field and density inhomogeneities are then further amplified once they cross the shock front, enhancing strong turbulence in the downstream region for $t \gtrsim 1.2 \times 10^3\,\Omega_L^{-1}$.

CR particles begin to be efficiently scattered at this stage, and the diffusive shock-acceleration process commences. Magnetic clumps provide the scattering centers, and most of the particles suffer multiple head-on collisions across the shock, resulting in a fractional energy gain. This process is best illustrated in Figure 9 where we show the spacetime diagram of one of the most energetic particles in the reference frame in which the shock is stationary. The color of the line indicates the particle energy as time advances while the background gray color map is created by superposing one-dimensional horizontal density profiles taken at the the particle's y coordinate.

In the top panel of Figure 10, we show the energy spectrum $Ef(E)$ as a function of the horizontal coordinate x and energy
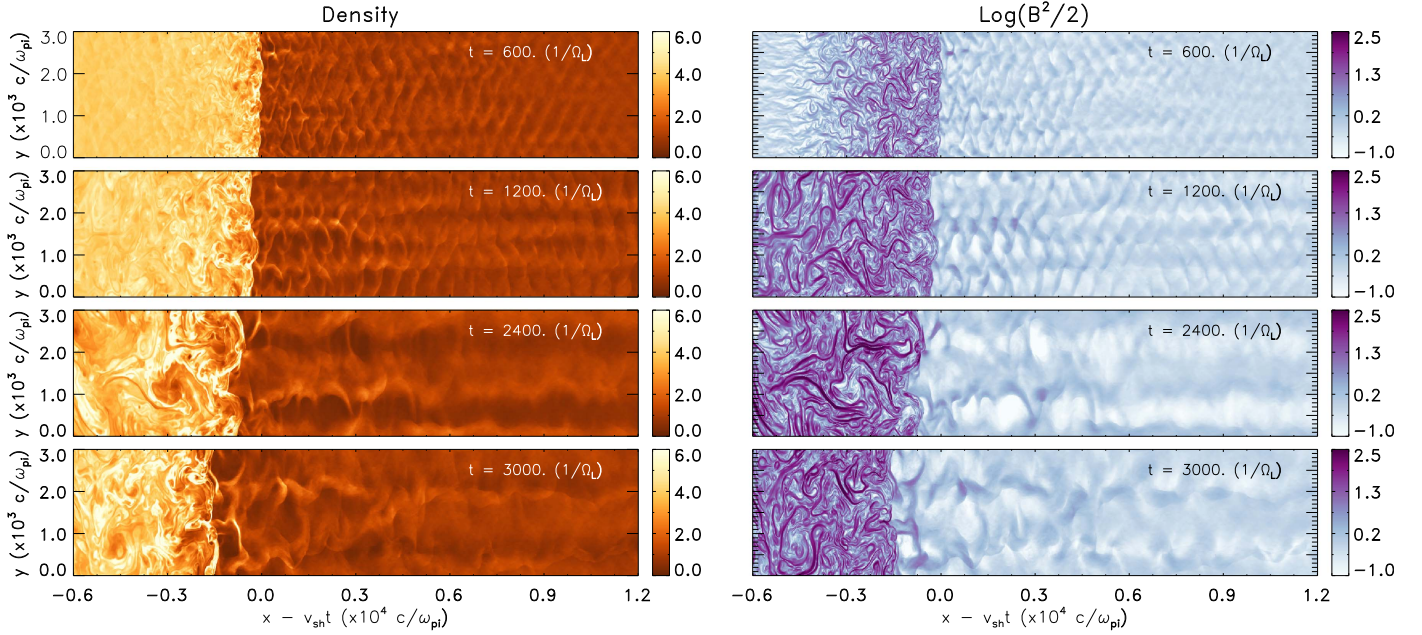
Figure 8. Density (left) and magnetic pressure (in log scale, right) snapshots for the collisionless shock problem (run R2) at four different times (reported in the panels). Only a small portion of the domain, in the proximity of the unperturbed shock position $x_s = v_{sh}t$, is shown.
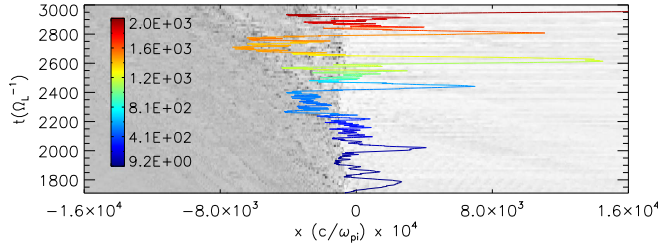
Figure 9. Spacetime diagram in the (x, t) plane showing the particle acceleration process. The line gives the particle trajectory, and the color indicates its specific kinetic energy. The background map in gray shows the y-averaged density structure of the system at different times.
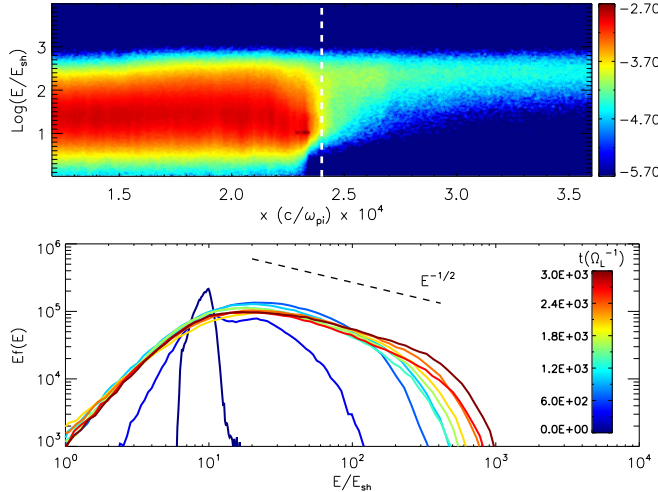
Figure 10. Top panel: particle energy distribution (in units of $E_{sh} = v_0^2/2$) as a function of x at $t = 2400\Omega_L^{-1}$ for the nonrelativistic run R2. The white vertical dashed line gives the (unperturbed) position of the shock front. Only a small region around the shock is shown. Bottom panel: time evolution of the particle energy spectrum $Ef(E)$ as a function of E. The different colors correspond to different simulation times, and the spectrum is extracted by considering particles lying in a narrow strip of width $\approx 800 \, c/\omega_{pi}$ in the downstream region. The black dashed line shows the slope predicted by the Fermi acceleration model.

E (in units of E_{sh}) at $t = 2400 \, \Omega_L^{-1}$. The two-dimensional distribution is constructed by taking, for each x coordinate, the spectra of all particles lying in a narrow vertical strip that is four zones wide. A tail of high-energy particles penetrating into the shock upstream and driving the Bell instability is visible, in agreement with previous results (see, e.g., Caprioli & Spitkovsky 2014a; Bai et al. 2015, and references therein). Note that since our injection procedure tracks the shock front more accurately, no artificial protrusion appears for $E \approx 10 E_{sh}$.

The particle spectrum is extracted from a narrow strip $[x_L, x_L + \delta]$ behind the shock, where $x_L = x_s - 2400 \, c/\omega_{pi}$ while $\delta = 800 \, c/\omega_{pi}$. The distribution function is normalized to the number of particles, i.e., $\int f(E)dE = N_{[x_L, x_L+\delta]}$. For isotropic scattering, the expected particle distribution $f(E)$ should depend only on the compression ratio r and take the form $f(E) \sim E^{(1-q)/2}$, where $q = 3r/(r-1)$. In the limit of strong shocks, one obtains $Ef(E) \sim E^{-1/2}$, and this prediction is confirmed by the time evolution of the energy spectrum plotted at different times in the bottom panel of Figure 10. The plot indicates that the CR spectrum gradually broadens from the injected distribution (dark blue curve peaked around $\sim 10 E_{sh}$) toward a high-energy power-law tail with a slope consistent with $-3/2$. A high-energy cutoff at $\sim 10^3 E_{sh}$ is reached toward the end of the simulation, in agreement with previous findings (see, e.g., Caprioli & Spitkovsky 2013, 2014a) and with the results of Bai et al. (2015).

4.5.3. Relativistic Regime

We have further investigated the diffusive shock-acceleration mechanism in the relativistic regime by repeating the R2-REL run discussed in Bai et al. (2015). A reduced value of the speed of light ($\mathbb{C} = 10\sqrt{2} \, v_0$) has been chosen in order to favor the transition from a nonrelativistic injection condition to the final acceleration stage, where the most energetic particles become
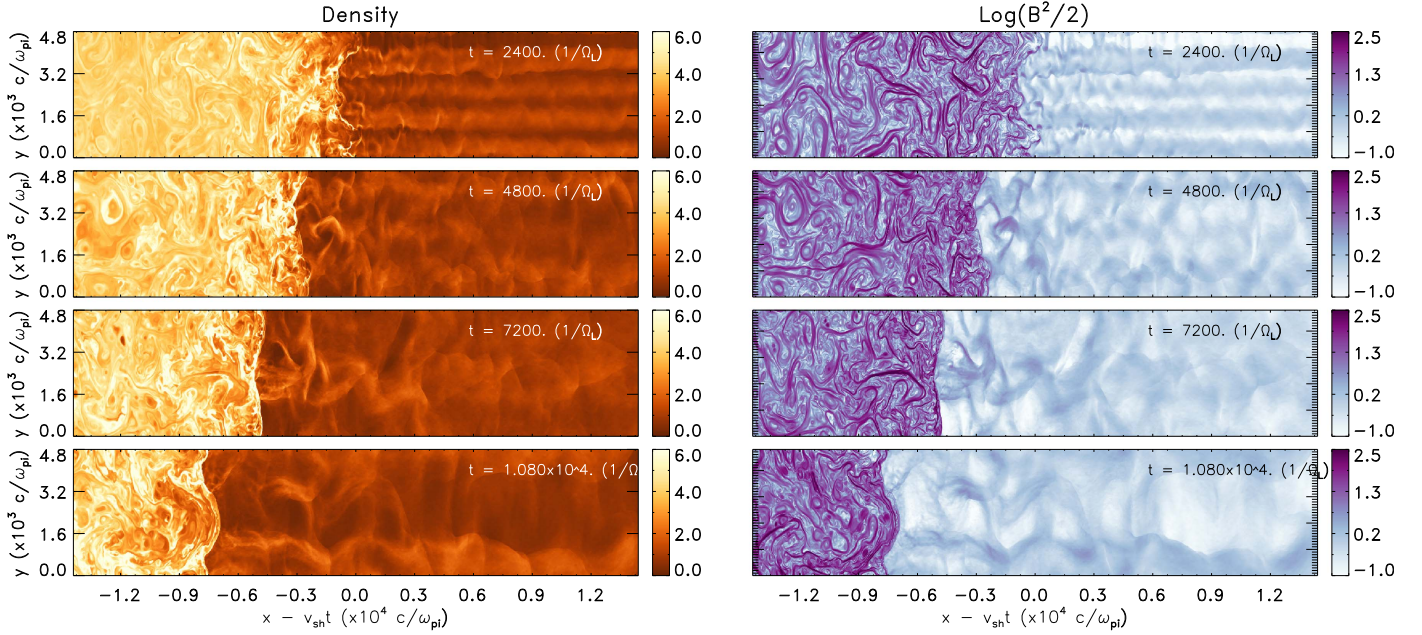
Figure 11. Density (left) and magnetic pressure (in log scale, right) snapshots for the collisionless shock problem in the relativistic run R2-REL at four different times (reported in the titles). Shown here is only a small portion of the domain centered around the unperturbed shock position $x_s = v_s t$.

relativistic. The typical particle velocity at injection is, indeed, $v_p = \sqrt{10}\, v_0 \approx 0.22\mathbb{C}$, corresponding to $\gamma_p \approx 1.026$. The transition to the relativistic regime occurs at approximately $E_t \approx \mathbb{C}^2/2$ when $\gamma_t \approx 1.5$.

The density and magnetic field strength are shown in the left and right panels of Figure 11 at different times. Upstream of the shock, we observe the formation of cavities and filamentary structures of larger size when compared to run R2, motivating the choice of a larger computational box. This behavior can be attributed to the saturation of the CR current density, which depends on the velocity of the particles and, for a reduced value of the speed of light, cannot exceed $q_{CR}\mathbb{C}$. In other words, at relativistic velocities, an increase in the particles' energy does not correspond to an increase in the current density. Indeed, from the linear analysis of the Bell instability (Equation (65)), we expect the most unstable wavenumber to be smaller in the relativistic case. Similarly, the level of turbulence is somewhat reduced, and a sharper shock transition layer is formed, in agreement with the results of Bai et al. (2015).

As a significant fraction of the fluid energy is transferred to CRs during the acceleration process, the effective adiabatic index of the fluid decreases from its nominal value of 5/3 (see Section 6.2 of Caprioli & Spitkovsky 2014a for a thorough discussion) to a smaller value $\tilde{\gamma}$. As a consequence, the shock compression ratio becomes slightly larger ($r \approx 4.2$) toward the end of the simulation. In addition, since we expect $v_{\rm sh} = -(\tilde{\gamma} - 1)/2v_0$ to hold for a strong shock, the front slows down and straggles with respect to its nominal position. This can be clearly observed in the snapshot sequence in Figure 11.

The energy and momentum distributions of CRs are shown in the three panels of Figure 12. In the top panel, we show a 2D color map of the spatial distribution of $Ef(E)$ at $t \approx 11,088\,\Omega_L^{-1}$ obtained by averaging, for each x, particles lying in a narrow vertical strip eight zones wide. From the figure, we see that most particles escaping into the upstream region have energy in excess of $10^2 E_{\rm sh}$ ($\gamma_p \gtrsim 1.25$). Again,
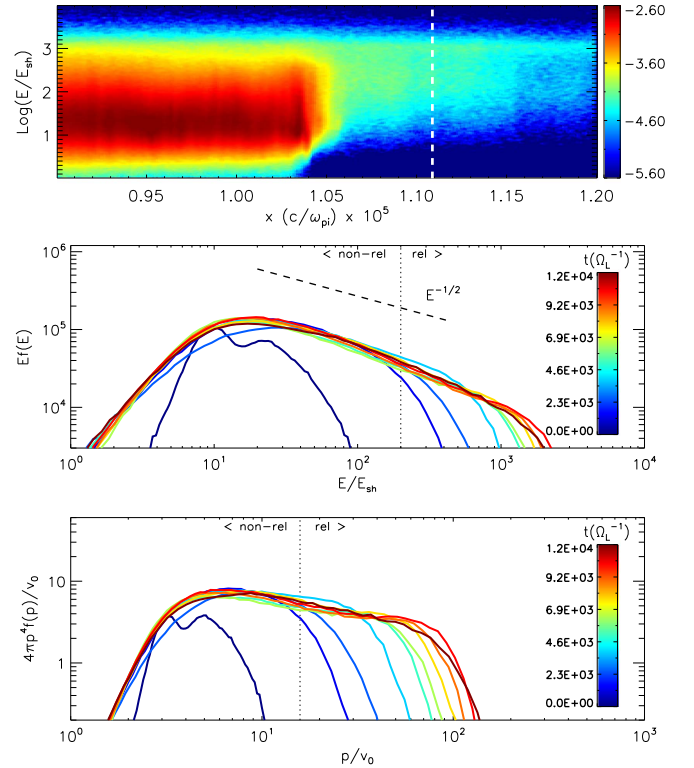
Figure 12. Top: spatial distribution of the particle energy (in units of $E_{\rm sh} = v_0^2/2$) as a function of x and E at $\Omega_L t = 11,088$. The white vertical dashed line gives the (unperturbed) position of the shock front. Only a smaller region around the shock is shown. Middle panel: time history of the energy spectrum $Ef(E)$ in dimensionless form. Curves with different colors correspond to the times indicated by the legend. Bottom panel: momentum spectrum $p^4 f(p)$ as a function of p/v_0. The thin vertical dotted lines mark the transition from nonrelativistic ($E \lesssim \mathbb{C}^2/2$) to relativistic energies ($E \gtrsim \mathbb{C}^2/2$) while the black dashed line in the top panel represents the theoretical expected slope in the classical regime.

since particle injection tracks more accurately the location of the shock front, we do not observe any low-energy protrusion in the upstream region.

In the middle panel of Figure 12, we plot the time history of the energy spectrum extracted by averaging, as before, all CR particles lying in a narrow strip located at a distance $\approx 2400\, c/\omega_{pi}$ behind the actual shock position. The spectrum is again consistent with a power law with spectral index $-3/2$, and presents a cutoff at $E \approx 2 \times 10^3$ ($\gamma \approx 3.5$). Note that a thin vertical line marks the transition from the nonrelativistic to relativistic energies ($E_t \approx \mathbb{C}^2/2$).

We also compute the momentum spectrum $f(p)$, which is related to the energy distribution $f(E)$ through the transformation

$$f(E_k) = 4\pi p^2 f(p) \frac{dp}{dE_k}, \qquad (78)$$

where $p \equiv \gamma_p v_p$ is the particle momentum per unit mass, while

$$E_k = (\gamma - 1)\mathbb{C}^2 = \mathbb{C}^2 \sqrt{1 + \left(\frac{p}{\mathbb{C}}\right)^2} - \mathbb{C}^2 \qquad (79)$$

is the specific kinetic energy. Using $dE_k/dp = p\mathbb{C}^2 / (E_k + \mathbb{C}^2)$, we invert Equation (78) to obtain $f(p)$ and plot the time history in the bottom panel of Figure 12. The figure shows $p^4 f(p)/v_0$ as a function of p and reveals an approximately flat curve in the region $p/v_0 \lesssim 15.8$ (the nonrelativistic region) and in $p/v_0 \gtrsim 25$ (the relativistic region).

We remind the reader that the Fermi acceleration theory predicts that the momentum spectrum should scale universally as $f(p) \propto p^{-4}$ at relativistic and nonrelativistic energies. Then, from Equation (78), one expects the energy distribution to smoothly change slopes while shifting to higher energies:

$$f(E_k) \propto \begin{cases} E_k^{-3/2} & \text{if} \quad E_k \ll \mathbb{C}^2 \\ E_k^{-2} & \text{if} \quad E_k \gg \mathbb{C}^2 \end{cases} \qquad (80)$$

in the nonrelativistic and relativistic parts of the spectrum, respectively. The transition to $f(E) \propto E^{-2}$ should take place at $\gamma \approx 10$, but it cannot be captured by the present simulation since such high energies have not been reached yet.

4.6. Particle Acceleration near an X-point

Next we consider, as a proof of concept, test-particle acceleration near an X-type magnetic reconnection region. Relativistic magnetic reconnection in strongly magnetized environments has been pointed out (Sironi & Spitkovsky 2014) as an efficient particle acceleration process which may be able to account for high-energy nonthermal emission from PWNe (see, e.g., Cerutti et al. 2013, and references therein), active galactic nuclei (AGNs; see, e.g., Giannios 2013), and GRBs (McKinney & Uzdensky 2012).

Our setup is similar to that of Mori et al. (1998) and consists of a 2D computational square with $-2L \leqslant x, y \leqslant 2L$, threaded by magnetic and electric fields given by

$$\boldsymbol{B} = B_0\left(\frac{y}{L}, \frac{x}{L}, \frac{B_z}{B_0}\right), \quad \boldsymbol{E} = (0, 0, E_z), \qquad (81)$$

where $B_0 = 1$. We choose the Alfvén speed as our reference velocity and set the speed of light to be $\mathbb{C} = 100 v_A$. Lengths are normalized to the gyration radius v_A/Ω_L, and we set $L = 2 \times 10^3$. Computations are stopped at $t = 100$ and employ 512^2 grid zones with four particles per cell. The particle
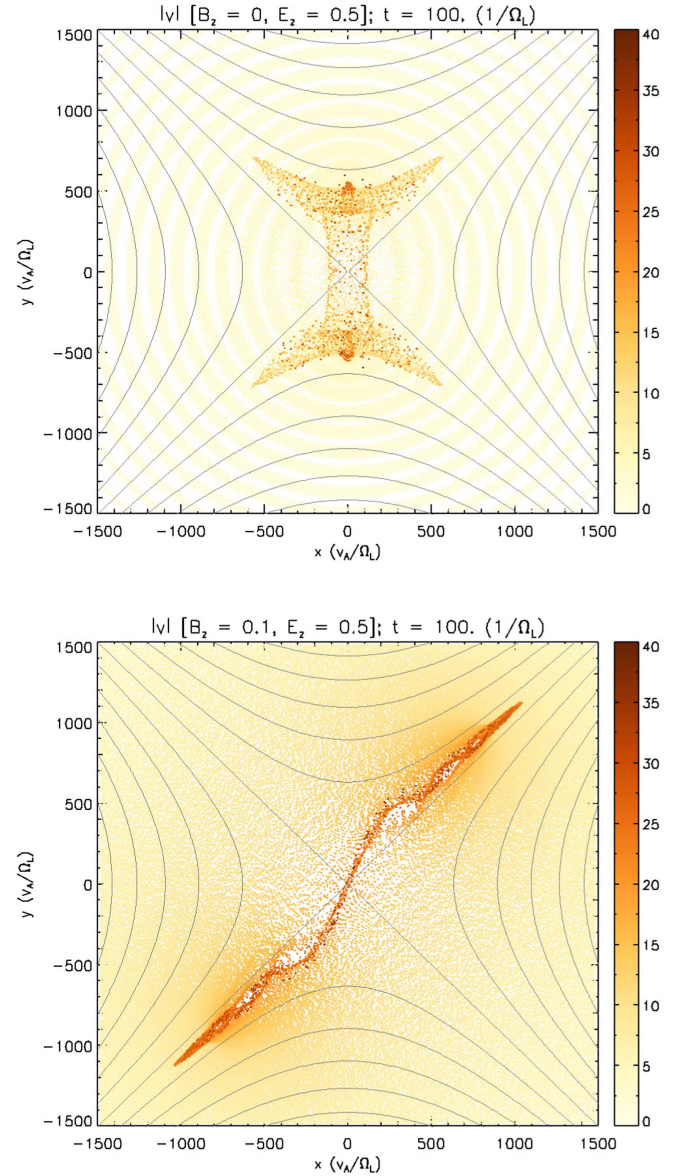

Figure 13. Test particle distribution for the X-point acceleration problem. Magnetic field lines in the x–y plane are drawn using black lines while particles are colored by velocity magnitude in orange. The top and bottom panels correspond, respectively, to the zero guide field case ($B_z = 0$) and to the guide field case with $B_z = 0.1$. In both cases, the electric field $E_z = 0.5$, directed out of the plane.

velocity distribution is initialized to a Maxwellian distribution with thermal velocity $0.1 v_A$. Only particles are evolved in time while fluid and electromagnetic quantities are kept constant at their initial values.

We first consider a configuration without a guide field ($B_z = 0$) and vary the electric field strengths according to $E_z = 0.1, 0.2, 0.3, 0.5, 1.0$. Since $\boldsymbol{E} \cdot \boldsymbol{B} = 0$ everywhere, particle acceleration takes place mostly in the proximity of the null point where the electric field has a larger amplitude than the magnetic field. Outside of this region, no significant acceleration occurs. Particle motion results from a combination of curvature, gradient, and $\boldsymbol{E} \times \boldsymbol{B}$ drifts, and produces a symmetric pattern with respect to the y axis, as shown in the top panel of Figure 13. Owing to the perpendicular electric drift, particles with a large velocity in the $|y| < |x|$ regions have a bouncing oscillatory motion between the two separatrices while
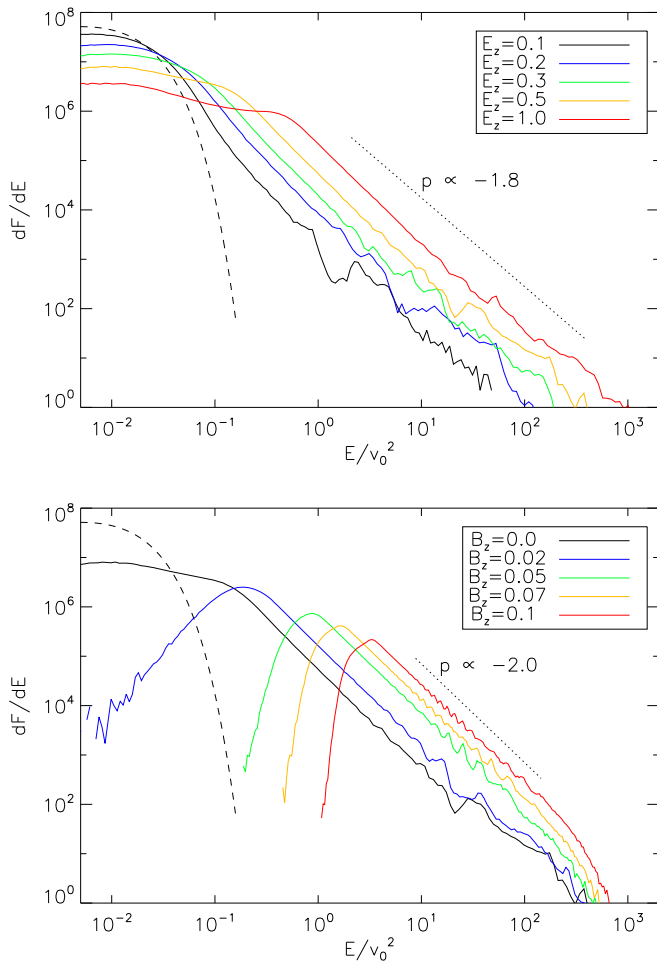
Figure 14. Particle energy spectra without (top panel) and with (bottom panel) the guide field. In the case with the guide field, the electric field E_z is set to 0.5. The dashed line indicates the initial Maxwellian distribution whereas the dotted line represents a power law with index -1.8 (top) and -2.0 (bottom).

approaching the central X-point (see Vekstein & Browning 1997; Browning & Vekstein 2001). In these regions, the curvature and gradient drift have opposite directions with respect to the electric field and are thus unfavorable for acceleration. Once the separatrix line is crossed, the situation is reversed and particles in the region $|y| > |x|$ move away from the null point because of the $\boldsymbol{E} \times \boldsymbol{B}$ drift. Concurrently, the curvature and gradient drift take place in the positive z direction, and particles gain energy due to the strong electric field, thus producing the pattern of higher energy particles observed in the top panel of Figure 13. A similar pattern is also shown by Mori et al. (1998). The energy spectrum, plotted in the top panel of Figure 14, shows a high-energy tail that departs from Maxwellian and extends to larger energies as the electric field is increased. For strong electric fields ($E_z \gtrsim 0.3$), we observe that the energy distribution can be well approximated with a power law $\propto E^{-p}$ with a spectral index $p \approx 1.8$ (for $E_z = 1$). This result is slightly smaller than the one found by Mori et al. (1998), who found $p \sim 2$.

In the second configuration, we fix the value of the electric field to $E_z = 0.5$ and repeat the computations using different values of the guide field, $B_z = 0, 0.02, 0.05, 0.07, 0.1$. The spatial distribution, shown in the bottom panel of Figure 13, indicates that the presence of a nonzero guide field breaks the symmetry with respect to the y axis, and the most energetic

particles are distributed on an elongated strip approximately lying along the separatrix line $y = x$, which is determined by the sign of the parallel components of the electric and magnetic fields. The same behavior has been reported by previous investigations, e.g., Browning & Vekstein (2001). As the guide field becomes stronger, parallel acceleration (as discussed in Section 4.2) increases and becomes significant. In fact, since $\boldsymbol{E} \cdot \boldsymbol{B} \neq 0$ everywhere, acceleration takes place for all particles including those away from the null point. This can be clearly seen in the energy spectra (bottom panel in Figure 14) showing a systematic shift to larger energies as the amplitude of the guide field grows. The effects of the perpendicular drift on the parallel motion still remain relevant so that the largest accelerations are observed close to the origin. However, the strength of the guide field seems to affect more the low-energy part of the spectra rather than the high-energy cutoff. Again, we observe that the high-energy tail of the spectrum behaves as a power law with spectral index (for $B_z = 0.1$) $p \sim 2$, in agreement with Mori et al. (1998).

4.7. Code Performance and Parallel Scaling

Let Δt_p and Δt_h be, respectively, the computational time required to update a single particle and a single grid zone using the MHD solver. The total CPU time for a single cell update may then be approximately expressed by

$$\Delta t = (m\Delta t_p + \Delta t_h), \tag{82}$$

where m is the number of particles per cell. In order to measure Δt_p, we have repeated the same computation with different values of m while leaving all other parameters unchanged so that

$$\Delta t_p \approx \frac{\Delta t_1 - \Delta t_2}{m_1 - m_2}, \tag{83}$$

where m_1 and m_2 are different numbers of particles per cell while Δt_1 and Δt_2 are the corresponding single-cell integration times. Code performance has been benchmarked on a 3 GHz Intel Xeon E5 processor using the relative drift test (Section 4.3) without subcycling and the grid resolution of 64 zones in each direction.

The left panel in Figure 15 shows the CPU time (in μs) computed using Equation (83) with and without the predictor step ("wp" and "np," respectively). As expected, the computational time is essentially independent of m and, on average, we find $\Delta t_p \approx 0.3~\mu$s (in 2D) and $\Delta t_p \approx 0.6~\mu$s (in 3D). We then include the predictor step (Section 3.2.1; blue symbols in the figure) and observe an average increase of $\sim$70%. The right panel of Figure 15 shows $m\Delta t_p/\Delta t$—the particle CPU time relative to a single cell update—as a function of m. With $m \approx 6 - 7$ particles per cell, the code spends $\approx$50% of the total computational time in evolving the particles (without the predictor step) in both 2D and 3D. Inclusion of the predictor step leads again to an increase of the relative cost.

The MHD–PIC module has been parallelized using the Message Passing Interface library. In our implementation, each processor updates only the particles lying in its physical domain (Vaidya et al. 2016). Particles must be transferred between neighbors when they cross a processor boundary: in this way, each processor communicates only with its neighbors. Parallel performance (in strong scaling) has been tested on the Marconi cluster equipped with Xeon Phi 7250 CPU (Knights
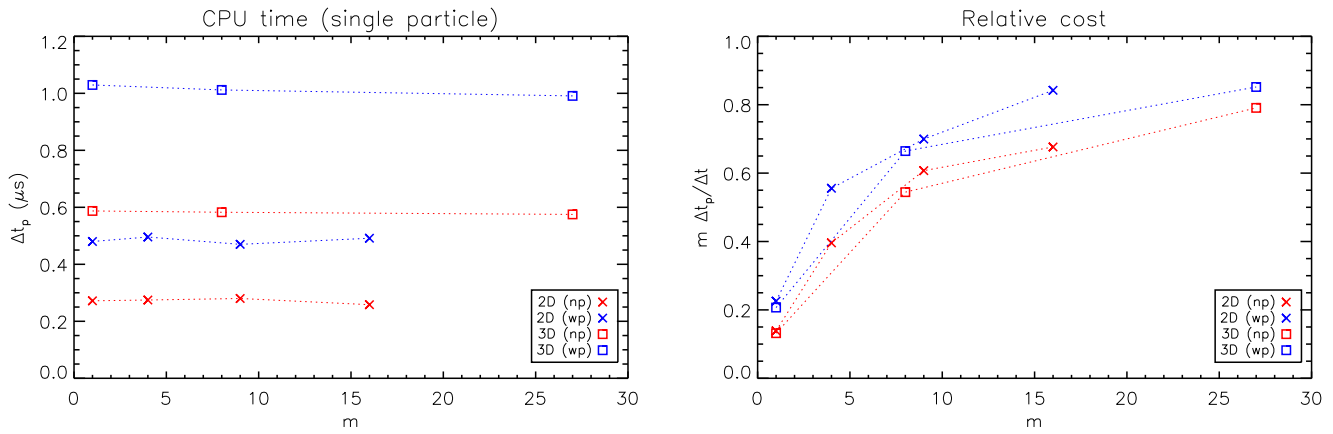
Figure 15. Left panel: single-particle CPU integration time (per time step) without the predictor (red symbols, "np") and with the predictor step (blue symbols, "wp"). Crosses (squares) correspond to 2D (3D) computations. Right: relative cost between particle integration time and overall CPU time for a single cell update.

Landing) processors at 1.40 GHz, available at the CINECA supercomputing facility. For the present scaling test, we have chosen the 3D Bell instability test problem (Section 4.4) with a grid resolution of 256×128^2, one particle per cell, and RK2 time stepping. Figure 16 plots the parallel efficiency, measured as $\Delta T_1/(p\Delta T_p)$ (where ΔT_p is the CPU time per step per zone using p processors), obtained for $p = 8, 16,\ldots1024$. The efficiency remains above ~0.8 up to $p \sim 256$ processors, and it decreases to ~0.7 at the largest number of processors. Note that, given the large inertia of CRs, the number of particles per cell remains constant throughout the computation. Numerical simulations with uneven particle distributions are likely to be less efficient.

5. Summary

A method paper describing a fluid–particle hybrid model for the dynamical interaction between a thermal plasma and a population of collisionless nonthermal particles (CRs) has been presented as part of the PLUTO code. The model equations can be formally derived starting from a three-component plasma in which thermal ions and (massless) electrons are combined together into a single fluid whereas the nonthermal component is treated kinetically. The single-fluid equations are those of MHD augmented by source terms accounting for the momentum and energy feedback from the CR particles. Ohm's law is derived from the electron equation of motion and, ignoring electron-scale physics, it is modified by the presence of the CR-induced Hall term, which accounts for the relative drift between the fluid and CRs. The resulting system of conservation laws is equivalent to the MHD–PIC equations previously derived by Bai et al. (2015). In the absence of momentum and energy feedback, the particle module can also be employed to investigate the dynamics of test particles embedded in an MHD fluid.

The MHD–PIC approach can be employed on scales that are much larger than the ion skin depth, thus offering a significant computational efficiency gain when compared to a PIC numerical approach. In this way, the MHD–PIC formalism paves the way for investigating kinetic effects at nearly macroscopic scales at a more affordable computational cost. At the same time, however, the formulation assumes that all electrons are thermal, and the charge density ratio between CR particles and fluid is required to be small. This limits the
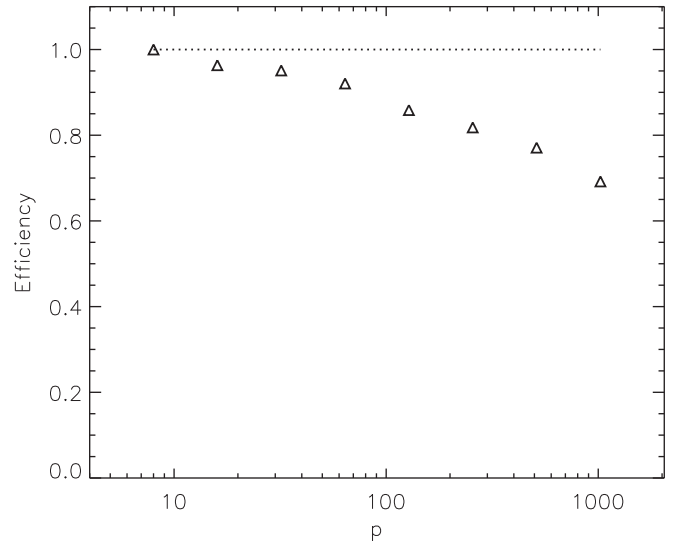
Figure 16. Parallel efficiency $E = \Delta T_1/(p\Delta T_p)$, where ΔT_p is the computational time obtained with p processors, and the normalization has been chosen so that $\Delta T_1 = 8\Delta T_8$. The test under consideration is the 3D Bell instability test problem with final integration time $t = 10$ and a resolution 256×128^2. The thin dotted line gives the ideal scaling ($E = 1$).

applicability of the model by compromising microphysical effects arising at scales smaller than the ion skin depth.

The system of equations describing the composite system of plasma and CRs is solved numerically by combining finite volume Godunov methods for the MHD fluid with PIC techniques for the particle component. In particular, we have presented a combined algorithm in which the fluid can be evolved using either the CTU method or Runge–Kutta time-marching schemes, both available in the PLUTO code. The particles' equations of motion are integrated using a second-order Boris pusher which is time reversible and features good conservation properties for long time simulations. When particle feedback is included, we have presented a modification of the Boris algorithm that preserves second-order accuracy in time. The correction consists of a predictor step where the electric field can be properly advanced at the half-time level, and it does not affect the time reversibility of the algorithm. Furthermore, we have suggested two novel particle subcycling algorithms that can be applied when the CR dynamical timescale becomes faster than the fluid evolution. By excluding particle feedback on the fluid, the same implementation can be

used to study test particles in a dynamically evolving or static fluid. The MHD–PIC model has been implemented in the PLUTO code for astrophysical plasma (Mignone et al. 2007, 2012), and it is part of a more general fluid/particle hybrid framework allowing different types of physics to be incorporated. A companion paper (Vaidya et al. 2018) describes yet another implementation for solving the CR transport equation of ultrarelativistic electrons with a time-dependent distribution.

We have verified our implementation through a number of numerical benchmarks including both test-particle dynamics in a fixed electromagnetic field or fully coupled evolution for the composite system (that is, with feedback). When possible, results obtained from numerical computations have been compared to analytical or reference solutions.

Test-particle configurations have been proposed in order to investigate CR trajectories in both orthogonal and parallel field configurations, reproducing the expected solution with very good accuracy. A simple benchmark configuration to inspect particle acceleration near a reconnecting X-point has been presented, confirming results from previously known studies (Vekstein & Browning 1997; Browning & Vekstein 2001).

The solution of the full MHD–PIC system of equations has been verified to be genuinely second-order accurate, and a numerical investigation of the nonresonant Bell instability in multiple spatial dimensions (Bell 2004) has shown excellent agreement with the results from linear analysis (Bai et al. 2015). The MHD–PIC model has been applied to investigate diffusive shock acceleration in 2D parallel MHD shocks. Since a nonthermal population of CRs cannot consistently originate from the thermal component within the proposed MHD–PIC framework, an "ad hoc" recipe to inject particles in the shock downstream has been proposed. The proposed injection method is more general than the one used by Bai et al. (2015) and can be extended to shocks with arbitrary shape, provided its energy can be specified. Being an imposed prescription, the injection process still depends on a free parameter (η) which controls the ratio between the mass of the generated CR particles and the mass swept by the shock. Our results reproduce, within statistical fluctuations, the findings of Bai et al. (2015), confirming that efficient acceleration takes place through Fermi mechanism. The system evolution is characterized by the development of strong turbulence, initially driven by the Bell instability in the shock precursors, accompanied by the formation of large cavities and filamentation and ensued by strong magnetic field amplification through the shock front. Particles become accelerated on a few thousands Larmor scales and, in the case of nonrelativistic particles, the resulting energy spectrum shows a power-law tail $f(E) \propto E^{-3/2}$. We have also investigated particle transition to the relativistic regime by considering a second simulation with a larger computational box and used a reduced value of the speed of light. Although the overall dynamical features are similar to the nonrelativistic case, the particle momentum spectrum behaves as $f(p) \propto p^{-4}$ as predicted by Fermi I acceleration. Our results are in agreement with the findings of previous authors, e.g., Caprioli & Spitkovsky (2014a) among others.

Our implementation will be made publicly available to the astrophysical community as a new particle module in the PLUTO code. Future extension of this work will take into account relativistic extension, more accurate injection recipes

enabling reconnection physics to be studied, and extension to adaptive grids.

Appendix A
Derivation of the MHD–PIC Equations

The fluid equations for ions and electrons can be obtained by taking moments of the distribution function directly from the Vlasov equations for the two species. The derivation can be found in many plasma physics textbooks (here we follow the book by Chiuderi & Velli 2015). We use the subscript s to denote the two species ($s = e, i$ for electrons and ions, respectively) with mass density $\rho^{(s)}$. The continuity, momentum, and energy equations for the two species take the form

$$\frac{\partial \rho^{(s)}}{\partial t} + \frac{\partial}{\partial x_k}(\rho v_k)^{(s)} = 0, \tag{84}$$

$$\frac{\partial}{\partial t}(\rho v_j)^{(s)} + \frac{\partial}{\partial x_k}(\rho v_j v_k + \mathcal{P}_{jk})^{(s)} - q^{(s)}E_j - q^{(s)}\left(\frac{\boldsymbol{v}^{(s)}}{c} \times \boldsymbol{B}\right)_j = 0, \tag{85}$$

$$\frac{\partial}{\partial t}\left(\frac{1}{2}\rho v^2 + \frac{\mathrm{Tr}(\mathcal{P})}{2}\right)^{(s)} + \frac{\partial}{\partial x_k} \times \left[\left(\frac{1}{2}\rho v^2 + \frac{\mathrm{Tr}(\mathcal{P})}{2}\right)v_k + v_j\mathcal{P}_{jk} + \mathcal{Q}_k\right]^{(s)} - q^{(s)}\boldsymbol{E}\cdot\boldsymbol{v}_i^{(s)} = 0, \tag{86}$$

where $\boldsymbol{v}^{(s)}$ is the average velocity, $q^{(s)}$ is the charge density, $\mathcal{Q}$ is the heat flux vector, $\boldsymbol{E}$ is the electric field, and $\boldsymbol{B}$ is the magnetic field. Equations (84)–(86) are written in terms of average velocity, defined as the first-order moment of the distribution function for the s species:

$$v_j^{(s)} = \langle V_j \rangle^{(s)}, \tag{87}$$

where V_j is the velocity coordinate in phase space and $\langle . \rangle^{(s)}$ represents the average taken over the distribution function of the s species. The pressure tensors and heat flux vector are defined in terms of the peculiar velocities $w_j^{(s)} = V_j - v_j^{(s)}$:

$$\mathcal{P}_{jk}^{(s)} = \rho^{(s)}\langle w_j w_k\rangle^{(s)}, \qquad \mathcal{Q}_k^{(s)} = \rho^{(s)}\left\langle \frac{w^2}{2}w_k\right\rangle^{(s)}. \tag{88}$$

Note that since $\boldsymbol{v}^{(e)}$ will in general be different from $\boldsymbol{v}^{(i)}$, the ion- and electron-pressure tensors as well as the heat flux vector are defined with respect to different fluid velocities.

In order to obtain the single-fluid equations, one needs to add the two momentum equations and likewise the two energy equations. In this process, however, the pressure tensors of the two species should be redefined so that the peculiar velocities

of the ions and electrons refer to the same fluid speed,

$$\mathbf{v} \equiv \mathbf{v}_g = \frac{\rho^{(e)}\mathbf{v}^{(e)} + \rho^{(i)}\mathbf{v}^{(i)}}{\rho^{(e)} + \rho^{(i)}}. \tag{89}$$

We thus need to redefine the peculiar velocities as $\mathbf{w}' = \mathbf{V} - \mathbf{v}_g$, implying that $\mathbf{w}'$ now has a nonzero mean:

$$\langle \mathbf{w}' \rangle^{(s)} = \mathbf{v}^{(s)} - \mathbf{v}_g \neq 0. \tag{90}$$

By adding the two momentum equations and the two energy equations, one arrives, after some algebra (for a detailed derivation, see Section 4.3 in the book by Chiuderi & Velli 2015), at

$$\frac{\partial \rho}{\partial t} + \frac{\partial}{\partial x_k}(\rho v_k) = 0, \tag{91}$$

$$\frac{\partial}{\partial t}(\rho v_j) + \frac{\partial}{\partial x_k}(\rho v_j v_k + \mathcal{P}'_{jk}) - q_g E_j$$
$$- \left(\frac{\mathbf{J}_g}{c} \times \mathbf{B}\right)_j = 0, \tag{92}$$

$$\frac{\partial}{\partial t}\left(\frac{1}{2}\rho v^2 + \frac{3}{2}P'\right)$$
$$+ \frac{\partial}{\partial x_k}\left[\left(\frac{1}{2}\rho v_g^2 + \frac{3}{2}P'\right)v_k + \mathcal{P}'_{jk}v_k + \mathcal{Q}'_k\right]$$
$$- \mathbf{J}_g \cdot \mathbf{E} = 0, \tag{93}$$

where

$$\rho = \rho^{(e)} + \rho^{(i)} \tag{94}$$

is the fluid density, while

$$q_g = q^{(e)} + q^{(i)}; \qquad \mathbf{J}_g = q^{(e)}\mathbf{v}^{(e)} + q^{(i)}\mathbf{v}^{(i)} \tag{95}$$

are the total charge density and current density, respectively. Note also that $q^{(e)} < 0$ while $q^{(i)} > 0$.

The total pressure tensor is now defined by the sum of the ion and electron tensors,

$$\mathcal{P}'_{jk} = \mathcal{P}'^{(e)}_{jk} + \mathcal{P}'^{(i)}_{jk} = P'\delta_{jk} + \Pi'_{jk}, \tag{96}$$

where each of the pressure tensors now refers to the the same fluid velocity, that is,

$$\mathcal{P}'^{(s)}_{jk} = \rho^{(s)} \langle w'_j w'_k \rangle^{(s)}. \tag{97}$$

A similar argument applies to the heat conduction flux, which is now given by $\mathcal{Q}'_k = \mathcal{Q}'^{(e)}_k + \mathcal{Q}'^{(i)}_k$ with $\mathcal{Q}'^{(s)}_k = \rho^{(s)} \langle (w')^2 w'_k \rangle^{(s)}/2$. In Equation (96), the pressure tensor has been decomposed, assuming isotropy, into a diagonal term containing the scalar pressure P' and the shear–stress tensor Π'_{jk} including only the off-diagonal terms which are different from zero in the presence of viscous forces.

Equivalence of the Pressure Tensors. We now prove that, in the limit of massless electrons, the two pressure tensors $\mathcal{P}'$ and $\mathcal{P}$ are actually equivalent. This statement can be proven by writing the single-fluid peculiar velocity as

$$\mathbf{w}' = \mathbf{V} - \mathbf{v}_g = \mathbf{w}^{(s)} + \delta\mathbf{v}^{(s)}, \tag{98}$$

where $\delta\mathbf{v}^{(s)} = \mathbf{v}^{(s)} - \mathbf{v}_g$, or more specifically,

$$\delta\mathbf{v}^{(i)} = \frac{\rho^{(e)}}{\rho}(\mathbf{v}^{(i)} - \mathbf{v}^{(e)}), \qquad \delta\mathbf{v}^{(e)} = \frac{\rho^{(i)}}{\rho}(\mathbf{v}^{(e)} - \mathbf{v}^{(i)}). \tag{99}$$

Equation (97) may now be written as

$$\mathcal{P}'^{(s)}_{jk} = \rho^{(s)}(\langle w_j w_k \rangle^{(s)} + \langle \delta v_j \delta v_k \rangle^{(s)})$$
$$= \mathcal{P}^{(s)}_{jk} + \rho^{(s)}\delta v_j^{(s)}\delta v_k^{(s)}. \tag{100}$$

Adding the two pressure tensors defined by Equation (100) gives

$$\mathcal{P}'_{jk} = \mathcal{P}^{(e)}_{jk} + \mathcal{P}^{(i)}_{jk} + \rho^{(e)}\delta v_j^{(e)}\delta v_k^{(e)} + \rho^{(i)}\delta v_j^{(i)}\delta v_k^{(i)}$$
$$= \mathcal{P}_{jk} + \frac{\rho^{(e)}\rho^{(i)}}{\rho}(v_j^{(i)} - v_j^{(e)})(v_k^{(i)} - v_k^{(e)}). \tag{101}$$

In the limit $\rho^{(e)} \to 0$, we thus obtain $\mathcal{P}_{jk} = \mathcal{P}'_{jk}$.

Appendix B
CTU–CT Integrator

We describe the implementation details of the CTU scheme combined with the CT method for the solution of the MHD–PIC equations in the PLUTO code. In what follows, we denote with $V = (\rho, \mathbf{v}_g, \mathbf{B}, p)$ and $U = (\rho, \rho\mathbf{v}_g, \mathbf{B}, E_g)$, respectively, the array of primitive and conservative variables. In the CTU–CT scheme (see, e.g., Gardiner & Stone 2005; Mignone et al. 2007), conservative variables such as density, momentum, and energy are stored as zone averages centered at the cell center $\mathbf{i} \equiv (i, j, k)$ while the magnetic field has a staggered representation so that the primary variables are defined at zone faces, i.e., $B_{x,i+\frac{1}{2}}$, $B_{y,j+\frac{1}{2}}$, and $B_{z,k+\frac{1}{2}}$. Note that, for the sake of clarity, we omit the integer subscripts i, j, and k when unnecessary and only keep the half-increment notation in denoting face values. The standard CTU–CT scheme must be modified in order to account for particle feedback during interface states computation, Riemann solver, and the final update stage.

1. At $t = t^n$, compute $\mathbf{F}^n_{CR}$ from the particles to the grid cell centers. This is done using Equation (14) with the current and charges obtained with Equation (22).
2. Compute normal predictors in primitive variables $V^*_{i,\pm}$ (at x faces), $V^*_{j,\pm}$ (at y faces), and $V^*_{k,\pm}$ (at z faces). In our notations, $V_{i,\pm} = \lim_{x \to x^\mp_{i\pm\frac{1}{2}}} V_i(x)$ denotes the rightmost $(+)$ and leftmost $(-)$ reconstructed value from within the cell. The reconstruction step can be carried out using either linear or piecewise parabolic interpolants; see Mignone et al. (2012) for details. The reconstruction is then followed by a time extrapolation step that can be performed in characteristic variables or using a simple Hancock step; see (for instance) Sections 3.2–3.3 of Mignone et al. (2012). For a simple second-order reconstruction in the x direction, for example, one has the formal correspondence

$$V^n_{i,\pm} = V^n \pm \frac{\delta_x V^n}{2}, \tag{102}$$

where $\delta_x V^n$ are limited slopes in the x direction. The normal predictor is then constructed (e.g., following a

MUSCL-Hancock scheme) as

$$V_{i,\pm}^* = V_{i,\pm}^n - \frac{\Delta t}{2\Delta x}\mathsf{A}\delta_x V^n, \tag{103}$$

where A is the Jacobian matrix of the one-dimensional primitive form of the equations (without CR contributions). The construction of the normal predictors in the y and z directions is done in a similar way.

3. Convert normal predictors in primitive variables to conservative ones $V_{i,\pm}^* \rightarrow U_{i,\pm}^*$ and add CR feedback terms to the momentum, magnetic field, and energy for a half-time step:

$$(\rho v)_{i,\pm}^* \leftarrow (\rho v)_{i,\pm}^* - \frac{\Delta t}{2}\boldsymbol{F}_{\mathrm{CR}}^n$$

$$\boldsymbol{B}_{i,\pm}^* \leftarrow \boldsymbol{B}_{i,\pm}^* + \frac{\Delta t}{2}\nabla_x \times \left(\frac{c\boldsymbol{F}_{\mathrm{CR}}^n}{q_i}\right)$$

$$E_{g,i,\pm}^* \leftarrow E_{g,i,\pm}^* - \frac{\Delta t}{2}\left[\nabla_x \cdot \left(\frac{c\boldsymbol{F}_{\mathrm{CR}}^n \times \boldsymbol{B}}{4\pi q_i}\right)\right)$$
$$+ \boldsymbol{F}_{\mathrm{CR}}^n \cdot v_g^n], \tag{104}$$

where $\nabla_x = (\partial_x, 0, 0)$ is the nabla operator in the x direction. Similar expressions hold for the y and z directions. Spatial derivatives are discretized using finite differences between the flux terms computed at the rightmost $(+)$ and leftmost $(-)$ interface values from within the cell, e.g.,

$$\frac{\partial F_{\mathrm{CR},z}^n}{\partial x} \approx \frac{(F_{\mathrm{CR},z}^n)_{i,+} - (F_{\mathrm{CR},z}^n)_{i,-}}{\Delta x}. \tag{105}$$

4. Solve a Riemann problem between normal predictors by means of a standard solver,

$$\mathcal{F}_{i+\frac{1}{2}}^* = \mathcal{R}(U_{i,+}^*, U_{i+1,-}^*), \tag{106}$$

and correct the magnetic field and energy fluxes to include contributions from CRs,

$$\mathcal{F}_{i+\frac{1}{2}}^{*,(B_y)} \leftarrow \mathcal{F}_{i+\frac{1}{2}}^{*,(B_y)} + \left(\frac{c F_{\mathrm{CR},z}^n}{q_g^n}\right)_{i+\frac{1}{2}}$$

$$\mathcal{F}_{i+\frac{1}{2}}^{*,(B_z)} \leftarrow \mathcal{F}_{i+\frac{1}{2}}^{*,(B_z)} - \left(\frac{c F_{\mathrm{CR},y}^n}{q_g^n}\right)_{i+\frac{1}{2}}$$

$$\mathcal{F}_{i+\frac{1}{2}}^{*,(E_g)} \leftarrow \mathcal{F}_{i+\frac{1}{2}}^{*,(E_g)} - \left[\frac{(c\boldsymbol{F}_{\mathrm{CR}}^n \times \boldsymbol{B}^n)_x}{4\pi q_i}\right]_{i+\frac{1}{2}}, \tag{107}$$

when computing fluxes in the x direction. The corrections are added by taking the upwind state depending on the sign of the density flux. Flux corrections in the y and z directions are obtained by cyclic permutations of the indices.

5. Evolve cell-centered values by half a time step:

$$U^{n+\frac{1}{2}} = U^n + \frac{\Delta t}{2}\sum_d \mathcal{L}_d^* + \frac{\Delta t}{2}S_{\mathrm{CR}}^n, \tag{108}$$

where $S_{\mathrm{CR}}^n = (0, -\boldsymbol{F}_{\mathrm{CR}}, 0, -\boldsymbol{F}_{\mathrm{CR}} \cdot v_g)^n$ is the CR source

term. In the previous equation,

$$\mathcal{L}_x^* = -\frac{\mathcal{F}_{i+\frac{1}{2}}^* - \mathcal{F}_{i-\frac{1}{2}}^*}{\Delta x}, \qquad \mathcal{L}_y^* = -\frac{\mathcal{F}_{j+\frac{1}{2}}^* - \mathcal{F}_{j-\frac{1}{2}}^*}{\Delta y},$$

$$\mathcal{L}_z^* = -\frac{\mathcal{F}_{k+\frac{1}{2}}^* - \mathcal{F}_{k-\frac{1}{2}}^*}{\Delta z}$$
$$\tag{109}$$

are the flux-difference right-hand side operators.

6. Advance the face-centered magnetic field by half a step:

$$B_{x,i+\frac{1}{2}}^{n+\frac{1}{2}} = B_{x,i+\frac{1}{2}}^n - \frac{\Delta t}{2\Delta y}(cE_{z,i+\frac{1}{2},j+\frac{1}{2}}^* - cE_{z,i+\frac{1}{2},j-\frac{1}{2}}^*)$$
$$+ \frac{\Delta t}{2\Delta z}(cE_{y,i+\frac{1}{2},k+\frac{1}{2}}^* - cE_{y,i+\frac{1}{2},k-\frac{1}{2}}^*)$$
$$B_{y,j+\frac{1}{2}}^{n+\frac{1}{2}} = B_{y,j+\frac{1}{2}}^n - \frac{\Delta t}{2\Delta z}(cE_{x,j+\frac{1}{2},k+\frac{1}{2}}^* - cE_{x,j+\frac{1}{2},k-\frac{1}{2}}^*)$$
$$+ \frac{\Delta t}{2\Delta x}(cE_{z,i+\frac{1}{2},j+\frac{1}{2}}^* - cE_{z,i-\frac{1}{2},j+\frac{1}{2}}^*)$$
$$B_{z,k+\frac{1}{2}}^{n+\frac{1}{2}} = B_{z,k+\frac{1}{2}}^n - \frac{\Delta t}{2\Delta x}(cE_{y,i+\frac{1}{2},k+\frac{1}{2}}^* - cE_{y,i-\frac{1}{2},k+\frac{1}{2}}^*)$$
$$+ \frac{\Delta t}{2\Delta y}(cE_{x,j+\frac{1}{2},k+\frac{1}{2}}^* - cE_{x,j-\frac{1}{2},k+\frac{1}{2}}^*). \tag{110}$$

In the previous equations, $c\boldsymbol{E}^*$ has been reconstructed from the face-centered fluxes computed at the predictor step (Equation (106)) to the cell edges by using a suitable reconstruction procedure. In the present work, we employ the UCT–Contact method by Gardiner & Stone (2005).

7. Advance particles by a full step using the algorithm described in Section 3.2. Also, compute the particle momentum and energy change over the time step and deposit them on the grid to obtain $S_{\mathrm{CR}}^{n+\frac{1}{2}}$ using Equation (25).

8. Correct states with transverse flux gradients to form corner-coupled states:

$$U_{i,\pm}^{n+\frac{1}{2}} = U_{i,\pm}^* + \frac{\Delta t}{2}\sum_{d\neq x} \mathcal{L}_d^*, \tag{111}$$

where the summation includes only the right-hand side operators in the transverse directions. Note that Equation (111) does not contain the source term since this has already been added in Equation (104). As usual, corner-coupled states in the y and z directions are obtained by suitable permutations.

9. Solve the Riemann problem between corner-coupled states,

$$\mathcal{F}_{i+\frac{1}{2}}^{n+\frac{1}{2}} = \mathcal{R}(U_{i,+}^{n+\frac{1}{2}}, U_{i+1,-}^{n+\frac{1}{2}}), \tag{112}$$

and correct fluxes in analogy with the predictor step, i.e., Equation (107).

10. Advance the zone-averaged conservative variables to the next time level,

$$U^{n+1} = U^n + \Delta t\sum_d \mathcal{L}_d^{n+\frac{1}{2}} + \Delta t S_{\mathrm{CR}}^{n+\frac{1}{2}}, \tag{113}$$

where $\mathcal{L}_d$ is obtained as in Equation (109) using the fluxes given by Equation (112).

11. Advance face-centered magnetic field to the next time level:

$$
\begin{aligned}
B_{x,i+\frac{1}{2}}^{n+1} &= B_{x,i+\frac{1}{2}}^{n} - \frac{\Delta t}{\Delta y}(cE_{z,i+\frac{1}{2},j+\frac{1}{2}}^{n+\frac{1}{2}} - cE_{z,i+\frac{1}{2},j-\frac{1}{2}}^{n+\frac{1}{2}}) \\
&\quad + \frac{\Delta t}{\Delta z}(cE_{y,i+\frac{1}{2},k+\frac{1}{2}}^{n+\frac{1}{2}} - cE_{y,i+\frac{1}{2},k-\frac{1}{2}}^{n+\frac{1}{2}}) \\
B_{y,j+\frac{1}{2}}^{n+1} &= B_{y,j+\frac{1}{2}}^{n} - \frac{\Delta t}{\Delta z}(cE_{x,j+\frac{1}{2},k+\frac{1}{2}}^{n+\frac{1}{2}} - cE_{x,j+\frac{1}{2},k-\frac{1}{2}}^{n+\frac{1}{2}}) \\
&\quad + \frac{\Delta t}{\Delta x}(cE_{z,i+\frac{1}{2},j+\frac{1}{2}}^{n+\frac{1}{2}} - cE_{z,i-\frac{1}{2},j+\frac{1}{2}}^{n+\frac{1}{2}}) \\
B_{z,k+\frac{1}{2}}^{n+1} &= B_{z,k+\frac{1}{2}}^{n} - \frac{\Delta t}{\Delta x}(cE_{y,i+\frac{1}{2},k+\frac{1}{2}}^{n+\frac{1}{2}} - cE_{y,i-\frac{1}{2},k+\frac{1}{2}}^{n+\frac{1}{2}}) \\
&\quad + \frac{\Delta t}{\Delta y}(cE_{x,j+\frac{1}{2},k+\frac{1}{2}}^{n+\frac{1}{2}} - cE_{x,j-\frac{1}{2},k+\frac{1}{2}}^{n+\frac{1}{2}}),
\end{aligned}
\tag{114}
$$

where $E^{n+\frac{1}{2}}$ has been reconstructed from the face-centered flux to the cell edges by using a suitable reconstruction procedure, e.g., Gardiner & Stone (2005).

ORCID iDs

G. Bodo https://orcid.org/0000-0002-9265-4081
B. Vaidya https://orcid.org/0000-0001-5424-0059

References

Amato, E., & Blasi, P. 2009, MNRAS, 392, 1591
Bai, X.-N., Caprioli, D., Sironi, L., & Spitkovsky, A. 2015, ApJ, 809, 55
Barniol Duran, R., Tchekhovskoy, A., & Giannios, D. 2017, MNRAS, 469, 4957
Bell, A. R. 2004, MNRAS, 353, 550
Bell, A. R. 2013, APh, 43, 56
Beniamini, P., & Giannios, D. 2017, MNRAS, 468, 3202
Beniamini, P., & Piran, T. 2014, MNRAS, 445, 3892
Birdsall, C., & Langdon, A. 2004, Plasma Physics via Computer Simulation, Series in Plasma Physics and Fluid Dynamics (London: Taylor and Francis)
Böttcher, M. 2007, Ap&SS, 309, 95
Browning, P. K., & Vekstein, G. E. 2001, JGR, 106, 18677
Bucciantini, N., Arons, J., & Amato, E. 2011, MNRAS, 410, 381
Caprioli, D., Pop, A.-R., & Spitkovsky, A. 2015, ApJL, 798, L28
Caprioli, D., & Spitkovsky, A. 2013, ApJL, 765, L20
Caprioli, D., & Spitkovsky, A. 2014a, ApJ, 783, 91
Caprioli, D., & Spitkovsky, A. 2014b, ApJ, 794, 47
Cerutti, B., Werner, G. R., Uzdensky, D. A., & Begelman, M. C. 2013, ApJ, 770, 147
Chang, P., Spitkovsky, A., & Arons, J. 2008, ApJ, 674, 378
Chiuderi, C., & Velli, M. 2015, Basics of Plasma Astrophysics (Milan: Springer)
Colella, P. 1990, JCoPh, 87, 171
Del Zanna, L., Volpi, D., Amato, E., & Bucciantini, N. 2006, A&A, 453, 621
English, W., Hardcastle, M. J., & Krause, M. G. H. 2016, MNRAS, 461, 2025
Gardiner, T. A., & Stone, J. M. 2005, JCoPh, 205, 509
Gargaté, L., Bingham, R., Fonseca, R. A., & Silva, L. O. 2007, CoPhC, 176, 419
Giannios, D. 2008, A&A, 480, 305
Giannios, D. 2013, MNRAS, 431, 355
Haugbølle, T., Frederiksen, J. T., & Nordlund, A. 2013, PhPl, 20, 062904
Kargaltsev, O., Cerutti, B., Lyubarsky, Y., & Striani, E. 2015, SSRv, 191, 391
Kunz, M. W., Stone, J. M., & Bai, X.-N. 2014, JCoPh, 259, 154
Landau, L. D., & Lifshitz, E. M. 1975, The Classical Theory of Fields (New York: Pergamon Press)
Lapenta, G. 2012, JCoPh, 231, 795
McKinney, J. C., & Uzdensky, D. A. 2012, MNRAS, 419, 573
Miceli, M., Orlando, S., Pereira, V., et al. 2016, A&A, 593, A26
Mignone, A., Bodo, G., Massaglia, S., et al. 2007, ApJS, 170, 228
Mignone, A., Rossi, P., Bodo, G., Ferrari, A., & Massaglia, S. 2010a, MNRAS, 402, 7
Mignone, A., Striani, E., Tavani, M., & Ferrari, A. 2013, MNRAS, 436, 1102
Mignone, A., & Tzeferacos, P. 2010, JCoPh, 229, 2117
Mignone, A., Tzeferacos, P., & Bodo, G. 2010b, JCoPh, 229, 5896
Mignone, A., Zanni, C., Tzeferacos, P., et al. 2012, ApJS, 198, 7
Mizuno, Y., Lyubarsky, Y., Nishikawa, K.-I., & Hardee, P. E. 2012, ApJ, 757, 16
Mori, K.-i., Sakai, J.-i., & Zhao, J. 1998, ApJ, 494, 430
Morlino, G., Blasi, P., Bandiera, R., Amato, E., & Caprioli, D. 2013, ApJ, 768, 148
Olmi, B., Del Zanna, L., Amato, E., Bucciantini, N., & Mignone, A. 2016, JPlPh, 82, 635820601
Orlando, S., Drake, J. J., & Laming, J. M. 2009, A&A, 493, 1049
Porth, O. 2013, MNRAS, 429, 2482
Rossi, P., Mignone, A., Bodo, G., Massaglia, S., & Ferrari, A. 2008, A&A, 488, 795
Sironi, L., & Spitkovsky, A. 2014, ApJL, 783, L21
Sironi, L., Spitkovsky, A., & Arons, J. 2013, ApJ, 771, 54
Vaidya, B., Mignone, A., Bodo, G., & Massaglia, S. 2016, Journal of Physics Conference Series, 719, 012023
Vaidya, B., Mignone, A., Bodo, G., Rossi, P., & Massaglia, S. 2018, ApJS, submitted
van Marle, A. J., Casse, F., & Marcowith, A. 2018, MNRAS, 473, 3394
Vekstein, G. E., & Browning, P. K. 1997, PhPl, 4, 2261